Marine Structures 83 (2022) 103174

Contents lists available at ScienceDirect

Marine Structures

journal homepage: www.elsevier.com/locate/marstruc

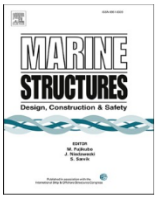

Hydrodynamic interaction of floating bridge pontoons and its effect on the bridge dynamic responses

Aksel Fenerci [a,*], Knut Andreas Kvåle [b], Xu Xiang [c], Ole Øiseth [b]

[a] Department of Ocean Operations and Civil Engineering, Norwegian University of Science and Technology, Norway
[b] Department of Structural Engineering, Norwegian University of Science and Technology, Norway
[c] Norwegian Public Roads Administration, Norway

ARTICLE INFO

Keywords:
Floating bridge
Pontoon
Hydrodynamic interaction
Diffraction
Radiation
Bridge dynamics

ABSTRACT

As pontoons of floating bridges respond to the dynamic actions of the wind and wave loading, additional forces are imposed on the pontoons due to the hydrodynamic interaction of these floating bodies. The wave forces on a selected pontoon and consequently its motion are affected by the presence and motion of adjacent pontoons through the motion of the fluid between the bodies. Here, we investigate the effect of such interactions on the global bridge dynamic responses. The hydrodynamic interaction effects are modeled using multibody potential theory with added artificial damping. The stochastic dynamic analyses of the bridge in the frequency-domain under combined wind and wave excitation revealed significant differences in the girder section forces when the interaction effects were included. The results imply that the hydrodynamic interaction effects should be considered in the design of such structures. The methodology presented here provides practical means for the analytical assessment of such effects.

1. Introduction

Floating bridges offer feasible alternatives when crossing wide straits to the more common cable-supported bridges, especially as the crossings get longer. In the cases where the bedrock lies deep which makes building classical pylons rather impractical, very long spans can be crossed using floating bridges. Despite its many advantages, floating bridges are much less common compared to cable-supported bridges. The longest floating bridge in the world as of today is the Evergreen Point Floating Bridge in Washington State, USA with its 2350 m span. Many other floating bridges with similar designs can be found in the Washington State (e.g. the Hood Canal Bridge), but other noteworthy examples can also be found elsewhere, such as the Demerera Harbour Bridge (1815 m, Guayana) or the Hobart Bridge (961 m, Australia). Solutions with both discrete and continuous pontoons exist, the latter being the most common. The longest discrete pontoon bridges without side-mooring can be found in Norway, namely the Bergsøysund and the Nordhordaland bridges. Further reading on floating bridges can be found elsewhere [1–5].

A floating pontoon bridge is planned in Norway for crossing the Bjørnafjord, which will be referred to hereafter as the Bjørnafjord Floating Bridge (BFB). The fjord crossing is 5 km wide and therefore calls a bridge that is significantly longer than the existing solutions. This, combined with the mountainous complex topography and the harsh environmental conditions typical of the region, makes the design of the bridge against the wind and wave actions a challenging engineering task. Moreover, there is a lack of experience and monitoring data from similar structures (except the work of [6] due to their scarcity. Consequently, utmost caution is

* Corresponding author.
E-mail address: aksel.fenerci@ntnu.no (A. Fenerci).

https://doi.org/10.1016/j.marstruc.2022.103174
Received 27 February 2021; Received in revised form 2 September 2021; Accepted 8 January 2022
Available online 7 February 2022

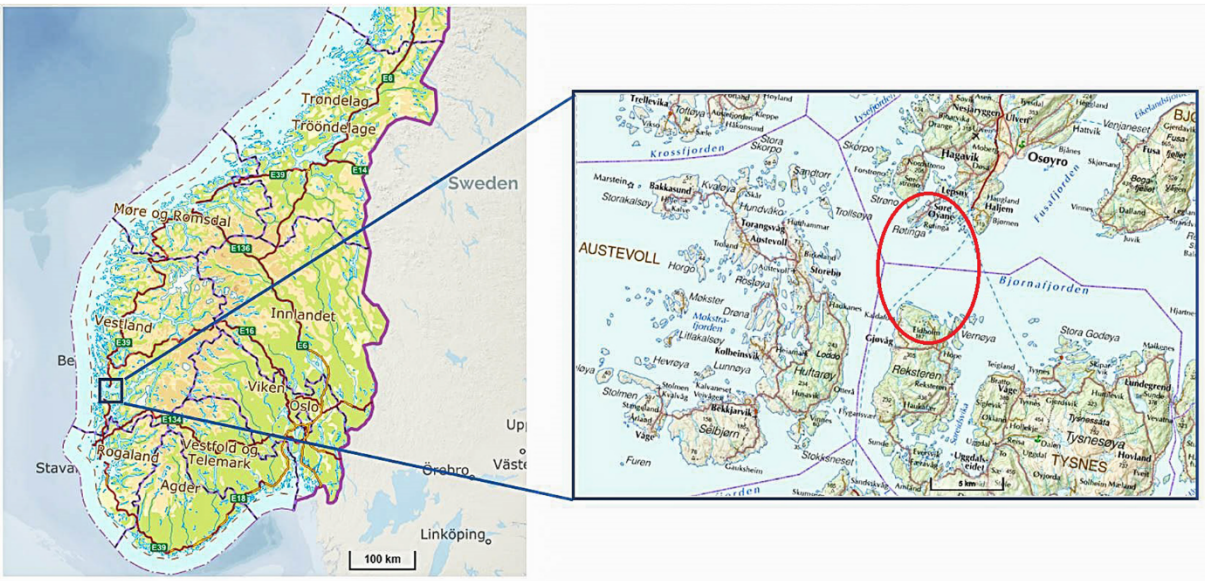

Fig. 1. Bjørnafjord, the geographical location of the future floating bridge.

required in the design stage, especially when handling dynamic phenomena. Dynamic effects due to wind and wave loads and the fluid-structure interaction should be modeled accurately for a good representation of the actual dynamic behavior. To that aim, stochastic dynamic analyses of these structures can be carried out using random vibration theory in either the time-domain [7–11] or the frequency-domain [2,12–15], where the latter requires that the nonlinearities in the system are omitted.

Accordingly, the dynamic effects on the bridge were investigated by the consultancy firms working on the concept development of the bridge. The reports including the dynamic analyses are now publicly available.[1] Besides, the dynamic response of the BFB was assessed by several researchers for earlier designs of the bridge [16–18]. The studies used commercial software to carry out time-domain simulations and focused on different issues such as the effect of inhomogeneous waves [19], wave directionality [18], pontoon optimization [20] and software-dependency [21]. Long-term extreme responses were assessed by Giske et al. [22] and Xu et al. [15]. Although most studies mentioned the potential effects of hydrodynamic interaction among the bridge pontoons, the studies neglected such interaction effects in their analyses.

Floating bodies in close proximity interact with each other such that the motion of a body is influenced by the presence of the adjacent bodies. It is well recognized that such an interaction can cause amplification of the dynamic response of the bodies due to resonant motion of the fluid between the bodies [23–28], a phenomenon also referred to as gap resonance [29–31]. The problem was highlighted in many early works and the theoretical background was outlined [27,32,33]; R.H.M [34,35]. In the context of marine operations, where side-by-side operations of large floating bodies such as ships, barges, or FPSOs are common, the hydrodynamic interaction effects and the consequent dynamic amplification or shielding effects in body responses were shown both experimentally and numerically [31,36–44]. When it comes to numerical analysis, although there are nuances in methodology, the most commonly used approach is to carry out potential flow analyses with artificial damping to account for viscous effects [30,38,44–46], which is calibrated using model tests or in rare occasions with CFD simulations. In most cases, the studies focused on very narrow gaps and parallel bodies but recent studies also present significant effects for wider gaps and non-parallel configurations [38].

In the case of floating bridges resting on discrete pontoons, hydrodynamic interaction effects on the bridge response can also be important, resulting in higher dynamic responses. This was highlighted by earlier works [10,16,47,48]. Despite the recognition of the potential effects, the issue has not been investigated yet, except the preliminary works of [48,49], where significant differences in global bridge responses due to pontoon interaction were reported. In these works, the authors have used commercial software and neglected viscous effects. Although the preliminary works are useful in understanding the potential effects, development of a fast and efficient framework is necessary for early assessment and quantification of such interaction effects. Here, we shall develop a such framework in frequency domain and introduce a method to account for viscous damping effects.

In this study, we present stochastic dynamic analyses of a super-long end-anchored floating pontoon bridge crossing the Bjørnafjord in Norway and focus on the influence of hydrodynamic interaction of the bridge pontoons. First, the bridge concept is described (Section 2) and the frequency-domain framework used in the analyses is introduced (Section 3). In sections 4 and 5, we present pontoon interaction effects using potential theory and their implementation to the framework, respectively. Section 6 summarizes the environmental load modeling and the analysis results are presented in Section 7. Important differences in the load effects are reported between the cases with and without interaction. The results are discussed critically considering their potential implications on bridge

---

[1] https://www.vegvesen.no/Europaveg/e39stordos/fjordkryssing-bjornafjorden/rapportar.

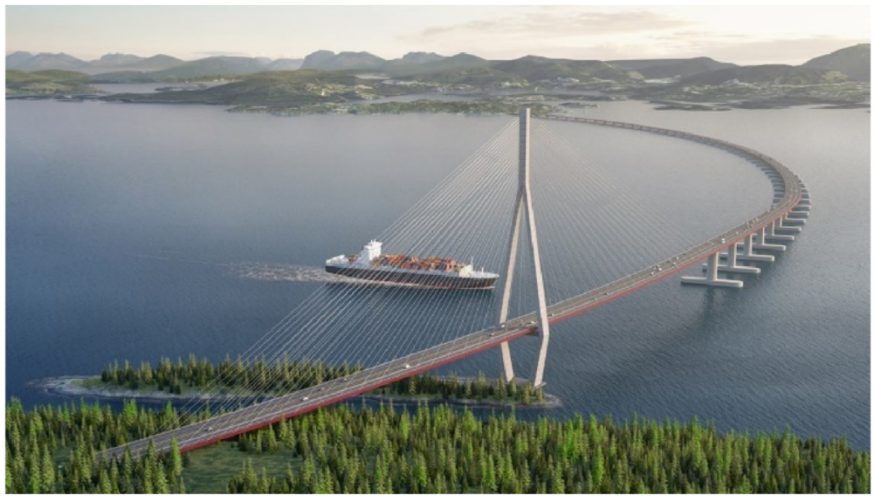

Fig. 2. Illustration of the Bjørnafjord Floating Bridge (courtesy of Statens vegvesen).

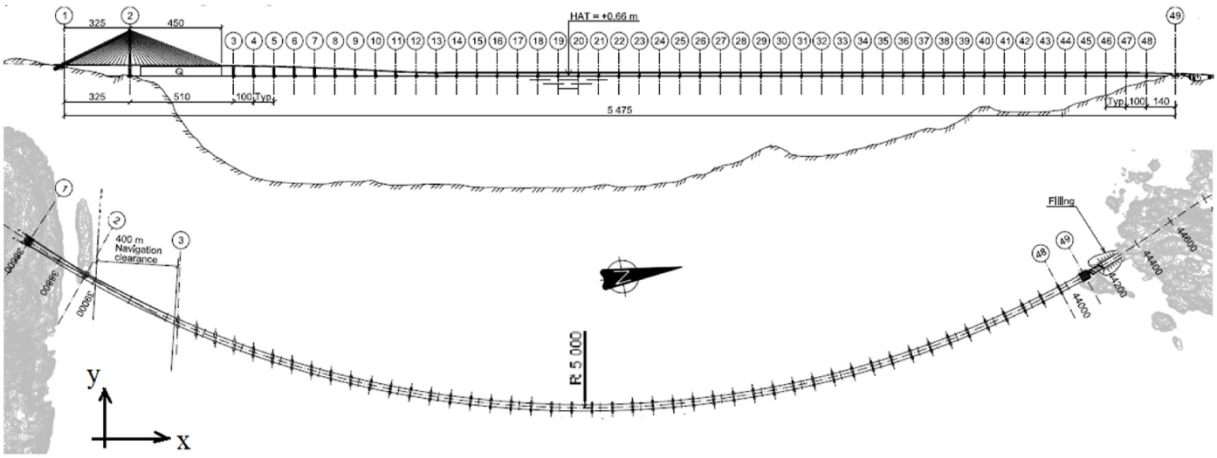

Fig. 3. Overview of the BFB (top: elevation view, bottom: plan view). Units are in meters.

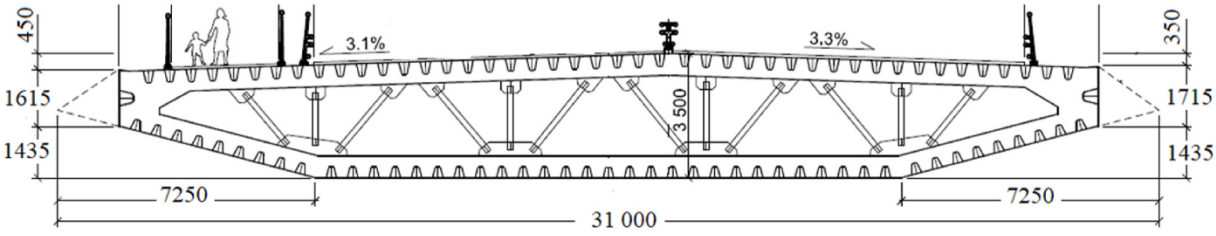

Fig. 4. Technical drawing of the bridge girder. Units are in mm.

design. The paper ends with a few concluding remarks.

2. Floating bridge over bjørnafjord

Norwegian Public Roads Administration (NPRA) is currently working on developing a floating bridge solution for crossing the 5 km wide Bjørnafjord. The Bjørnafjord lies at the west coast of Norway (Fig. 1) with little shelter from the North Sea. The local topography of the bridge site is complex, composed of steep mountains, small islands, and many fjord branches, a typical condition for the Norwegian fjords. Moreover, the environmental conditions, namely the current, wind, and the waves at the bridge site are quite harsh,

Table 1
Pontoon types in BFB.

type	P1	P2	P3	P4
Pontoons	1	2–4	5–10	11–46
Length (m)	58	58	58	58
Width (m)	16	14	12	10

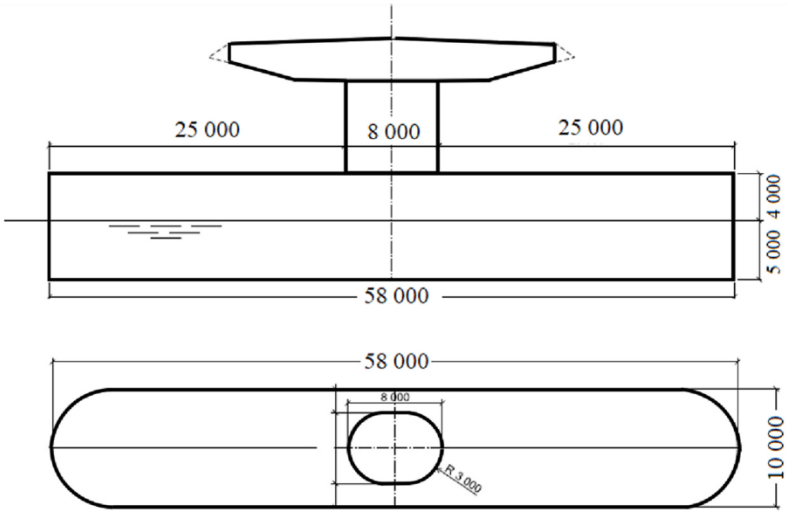

Fig. 5. Technical drawing of the low bridge pontoons (P4). Units are in mm. Top: elevation view. Bottom: plan view.

largely due to the North Sea exposure. Therefore, the Bjørnafjord Floating Bridge (BFB) is a unique structure both due to its colossal size and the environmental conditions it is subjected to.

The lack of experience from similar structures requires a very careful investigation of all possible effects on the dynamic behavior of the structure in the design stage since such phenomena can be more difficult to deal with after the project is realized. Here, an up-to-date design of the BFB will be considered to study the hydrodynamic interaction effects among the bridge pontoons. Since the concept development is ongoing, the detailed design is subjected to changes. The bridge concept is a curved deck with a radius of 5000 m that rests on 46 floating pontoons (Fig. 2-Fig. 3). The girder is a streamlined steel box girder, a type commonly used for wind-sensitive cable-supported bridges. The deck cross-section is shown in Fig. 4, which is only 31 m wide and 3.5 m high.

The south end of the bridge transitions into a cable-stayed high bridge with a clear span of 510 m to allow ship passage. There, the bridge deck is 55 m above sea level. Towards the north end, the bridge deck gradually lowers to 14 m above sea level. The bridge deck is supported by 46 stainless steel floating pontoons. The pontoon dimensions vary slightly from the high bridge to the low bridge and are given in Table 1. A detailed drawing of the low-bridge pontoon (P4) is given in Fig. 5.

3. Stochastic dynamic analysis of floating bridges

A floating pontoon bridge such as the BFB will be subjected to random dynamic excitation due to environmental actions comprised of wind and wave loads. In order to predict the dynamic response of the bridge to such loading with good accuracy, the dynamic properties of the structure, the aerodynamic and hydrodynamic loads, and the fluid-structure interaction should be modeled properly.

Owing to the random nature of the loading, the dynamic response of the bridge can only be evaluated stochastically based on the random vibration theory. Such an analysis can be carried out both in the frequency and time domains. When the nonlinearities such as geometrical or material nonlinearities or nonlinear forces can be neglected and the system can be described as linear and time-invariant, the frequency-domain approach is time-efficient and well-suited for modeling the fluid-structure interaction. Here, owing to small deflections and the aerodynamically linear girder, the system is linearized after the static loads are applied. A frequency domain framework is then adopted to evaluate the dynamic response of the BFB and study the effects of hydrodynamic interaction. The framework is largely adopted from Kvåle et al. [2]; which was further developed by Xu et al. [11] to include the wind effects. The possible effect of nonlinearities on the dynamic response of the bridge is considered out of scope of the study, where our focus is the hydrodynamic interaction of the bridge pontoons.

Our starting point is a finite element (FE) model of the bridge, which was created by the NPRA using ABAQUS FE [50] software (Fig. 6). The model is composed of the bridge deck, the tower, cables, pontoon columns, and pontoons. The deck, the tower, and the columns are modeled by B31 beam elements, which are 3D elements with 12 degrees-of-freedom and linear interpolation. The cables are modeled using simple cable elements. All degrees of freedom at the end nodes of the girder are fixed. The pontoons are modeled as

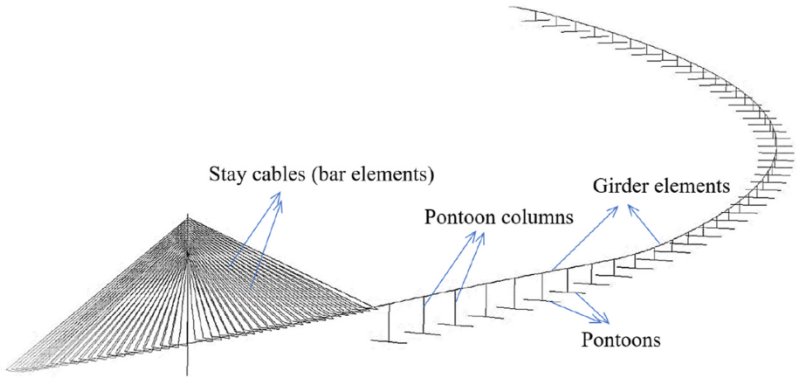

Fig. 6. Finite element model of the BFB.

Table 2
Properties of the bridge deck section.

Area (m^2)	1.43
Second moment of area (I_{11}) – weak axis (m^4)	2.67
Second moment of area (I_{22}) – strong axis (m^4)	114.83
J (m^4)	6.88
E (MPa)	2.10E+5
G (MPa)	8.08E+4

Table 3
Properties of the pontoon columns.

	P1	P2&P3	P4
Area (m^2)	1.75	1.15	0.67
I_{11} & I_{22} (m^4)	27.22	12.014	4.27
J (m^4)	54.436	24.03	8.54
E (MPa)	2.10E+5	2.10E+5	2.10E+5
G (MPa)	8.08E+4	8.08E+4	8.08E+4

Table 4
Hydrostatic stiffness and mass of the pontoons.

	P1	P2	P3	P4
mass (kg)	1,969,970	1441880	1273912	958856
K_{zz} (kN/m)	8.78E+03	7.74E+03	6.68E+03	5.61E+03
K_{mxx} (kN.m/rad)	8.27E+04	3.79E+04	3.22E+03	−1.66E+04
K_{myy} (kN.m/rad)	2.11E+06	1.89E+06	1.65E+06	1.40E+06

rigid beams to include their hydrostatic stiffness and mass contributions. The fluid-structure interaction will be modeled outside the FE model. The pontoon mass contributions are included using lumped masses at the pontoon locations. The hydrostatic stiffness of the pontoons is calculated from the buoyancy and modeled using additional "translational and rotational" springs at the pontoon nodes. The geometry and material input for the deck elements and the pontoon columns are given in.

Table 2 and Table 3, respectively. Note that the transverse axis of the girder section will be referred to as the weak axis (due to its lower bending stiffness) where the vertical axis will be referred to as the strong axis of the bridge girder section throughout the paper. The hydrostatic stiffness contributions due to the floating pontoons are given in Table 4.

3.1. Eigenvalue analysis

The system matrices in still-air and dry-pontoon conditions, namely the structural stiffness, mass, and damping matrices are assembled using the finite element method. The structural damping is modeled using Rayleigh damping with coefficients $\mu = 0.0009$, $\lambda = 0.01102$, for mass and stiffness, respectively. The classical eigenvalue problem is then solved to obtain the still-air dry mode shapes and frequencies of the structure. The first 30 vibration modes are summarized in Table 5 and a few first modes are plotted in Fig. 7.

Table 5
Still-air dry vibration modes of the BFB bridge.

Mode No	f (Hz)	T (s)	Motion[a]	mode no	f (Hz)	T (s)	Motion[a]
1	0.009223	108.43	H	16	0.20338	4.917	H
2	0.017115	58.427	H	17	0.21044	4.752	H
3	0.030574	32.708	H	18	0.21326	4.6892	V
4	0.043776	22.843	H	19	0.21724	4.6033	H
5	0.063739	15.689	H	20	0.22055	4.5341	V
6	0.075672	13.215	H	21	0.22447	4.455	V
7	0.092569	10.803	H	22	0.22467	4.4511	V
8	0.10827	9.2359	H	23	0.22468	4.4508	V
9	0.12236	8.1728	H	24	0.22472	4.4499	V
10	0.13517	7.3979	H	25	0.22474	4.4497	V
11	0.14456	6.9177	H	26	0.22484	4.4475	V
12	0.16564	6.0373	H	27	0.22513	4.4419	V
13	0.18368	5.4441	V	28	0.22549	4.4348	V
14	0.18929	5.2829	V	29	0.22606	4.4236	V
15	0.19696	5.0771	H	30	0.22649	4.4153	V

[a] H = horizontal mode, V = vertical mode, f:natural frequency, T: natural period.

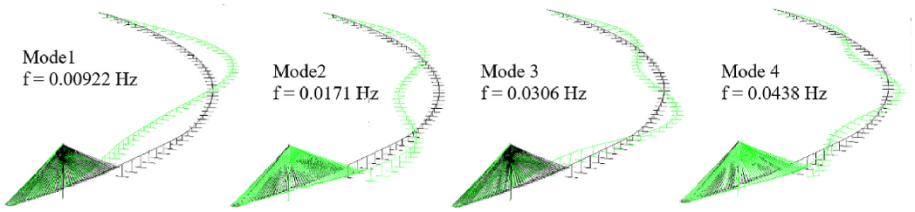

Fig. 7. Mode shapes of the BFB.

After obtaining the still-air dry mode shapes of the structure, the structural system matrices can be written in terms of the generalized coordinates of these mode shapes as

$$\widetilde{\mathbf{M}}_{\mathbf{s}} = \mathbf{\Phi}^T \mathbf{M}_{\mathbf{s}} \mathbf{\Phi},\ \widetilde{\mathbf{K}}_{\mathbf{s}} = \mathbf{\Phi}^T \mathbf{K}_{\mathbf{s}} \mathbf{\Phi},\ \widetilde{\mathbf{C}}_{\mathbf{s}} = \mu \widetilde{\mathbf{M}}_{\mathbf{s}} + \lambda \widetilde{\mathbf{K}}_{\mathbf{s}} \tag{1}$$

where $\mathbf{M_s}$, $\mathbf{K_s}$, and $\mathbf{C_s}$ are the structural mass, stiffness, and damping matrices and the hat indicates that the matrices are in generalized coordinates. $\mathbf{\Phi}$ is the mode shape matrix.

3.2. Hydrodynamic loads

The hydrodynamic loads acting on floating bodies such as the BFB pontoons can be modeled as a superposition of the so-called Froude-Krylov, diffraction, and radiation forces. The former two represent the forces on the fixed body due to the incident and the diffracted waves, respectively. The superposition of these two forces will be referred to as the wave excitation forces, which can be described in terms of a spectral density matrix as follows:

$$\mathbf{S}_{pp}(\omega) = \begin{bmatrix} S_{p_1 p_1} & \cdots & S_{p_1 p_m} \\ \vdots & \ddots & \\ S_{p_n p_1} & & S_{p_n p_m} \end{bmatrix},\ \mathbf{S}_{p_n p_m}(\omega) = \int_{\theta} \mathbf{\Theta}_n(\omega,\ \theta) S_{\eta_n \eta_m}(\omega,\ \theta) \mathbf{\Theta}_m{}^H(\omega, \theta) d\theta \tag{2}$$

where $\mathbf{\Theta}_n(\omega, \theta)$ denotes the wave excitation transfer function for pontoon n and $(..)^H$ is the Hermitian transpose. The cross-spectral density of the wave elevation $S_{\eta_n \eta_m}$ can be written for each pontoon pair as

$$S_{\eta_n \eta_m} = \int_{-\pi}^{\pi} S_{\eta}(\omega) D(\theta - \theta_0) e^{\left(-i \frac{|\omega|\omega}{g} (\Delta x_{nm} \cos\theta + \Delta y_{nm} \sin\theta) \right)} d\theta,\ \Delta x_{nm} = |x_n - x_m| \tag{3}$$

where $S_{\eta}(\omega)$ is the one-dimensional wave elevation spectrum and $D(\theta)$ is the directional spectrum. Further, θ_0 denotes the mean wave direction, where Δx_{nm} and Δy_{nm} denote the distances between pontoons n and m. The cross-spectral density matrix of the wave excitation forces can also be written in generalized coordinates as follows:

$$\widetilde{\mathbf{S}}_{\mathbf{p}}(\omega) = \mathbf{\Phi}_{hydro}^{T}\mathbf{T}_{pont}^{T}\mathbf{S}_{pp}(\omega)\mathbf{T}_{pont}\mathbf{\Phi}_{hydro},\ \mathbf{T}_{pont} = \begin{bmatrix} \mathbf{T}_{pont}^{1} & & \mathbf{0} \\ & \ddots & \\ \mathbf{0} & & \mathbf{T}_{pont}^{n} \end{bmatrix} \tag{4}$$

Here, the cross-spectral density matrix is first transformed to the global FE coordinates from the local pontoon coordinates using $\mathbf{T}_{pont}$ and then transformed to the generalized coordinates using $\mathbf{\Phi}_{hydro}$, which is the mode shape matrix of the pontoon degrees-of-freedom.

The remaining radiation forces are motion-dependent and commonly represented using frequency-dependent added mass ($\mathbf{M_h}(\omega)$) and damping ($\mathbf{C_h}(\omega)$) matrices. The 6 × 6 matrices $\mathbf{M}_h^n(\omega)$ and $\mathbf{C}_h^n(\omega)$ for each pontoon n are first transformed and assembled to the global degrees-of-freedom of the FE model as

$$\mathbf{M_h}(\omega) = \sum_{n=1}^{N_p}\left(\mathbf{T}_{pont}^{n}\right)^{T}\mathbf{M}_h^n(\omega)\left(\mathbf{T}_{pont}^{n}\right),\ \mathbf{C_h}(\omega) = \sum_{n=1}^{N_p}\left(\mathbf{T}_{pont}^{n}\right)^{T}\mathbf{C}_h^n(\omega)\left(\mathbf{T}_{pont}^{n}\right) \tag{5}$$

Then, the matrices in generalized coordinates will read:

$$\widetilde{\mathbf{M}}_{\mathbf{h}}(\omega) = \mathbf{\Phi}_{hydro}^{T}\mathbf{M_h}(\omega)\mathbf{\Phi}_{hydro},\ \widetilde{\mathbf{C}}_{\mathbf{h}}(\omega) = \mathbf{\Phi}_{hydro}^{T}\mathbf{C_h}(\omega)\mathbf{\Phi}_{hydro} \tag{6}$$

3.3. Aerodynamic loads

Aerodynamic loads acting on the structure are composed of the so-called buffeting loading due to the wind turbulence and the self-excited forces which occur as a result of the motion of the bridge deck submerged in the moving air. Neglecting the aerodynamic admittance, the buffeting forces for acting on a section of a beam element can be written as:

$$\mathbf{q}(t) = \mathbf{B_q}\mathbf{T}_{w1}\mathbf{V}(t),\ \mathbf{B_q} = \frac{\rho U B}{2}\begin{bmatrix} 0 & 0 & 0 \\ 0 & 2(D/B)C_D & (D/B)C_D^{'} - C_L \\ 0 & 2C_L & C_L^{'} + (D/B)C_D \\ 0 & -2BC_M & -BC_M^{'} \\ 0 & 0 & 0 \\ 0 & 0 & 0 \end{bmatrix},\ \mathbf{V}(t) = \begin{bmatrix} u(t) \\ v(t) \\ w(t) \end{bmatrix} \tag{7}$$

Here, $\mathbf{T}_{w1}$ is the transformation matrix between the wind coordinate system and the local coordinate system of the beam element. The wind coordinate system is a cartesian coordinate system defined by the three turbulence components $\{u, v, w\}$ where u is directed at the mean wind direction. C_D, C_L, C_M denote the drag, lift, and moment coefficients for the section where $C_D^{'}, C_L^{'}, C_M^{'}$ are their derivatives with respect to the angle-of-attack. ρ, U, B and D are the air density, mean wind speed, and the width and the height of the section, respectively. The buffeting forces acting on the degrees-of-freedom of the beam element can then be obtained using the finite element formulation:

$$\mathbf{Q}_{buff}^{el}(t) = \mathbf{G}\mathbf{B_q}\mathbf{T}_{w1}\mathbf{V}(t),\ \mathbf{G} = \int_0^{L_{el}}\mathbf{N}^{T}(x)dx \tag{8}$$

where $\mathbf{N}(x)$ is the matrix of shape functions and L_{el} is the length of the beam element. It is assumed that the mean wind speed and the section properties are constant along the element. The spectral density matrix of the buffeting forces in the global FE coordinates of the structure can then be assembled by summing up the contributions from each beam element as follows:

$$\mathbf{S_{qq}}(\omega) = \sum_{n=1}^{N_{el}}\sum_{m=1}^{N_{el}}\mathbf{T}_{w2}^{n}\mathbf{G}^{n}\mathbf{B_q}^{n}\mathbf{T}_{w1}^{n}\mathbf{S_V}(x_n, x_m, \omega)\left(\mathbf{T}_{w1}^{m}\right)^{T}\left(\mathbf{B_q^m}\right)^{T}(\mathbf{G}^{m})^{T}\left(\mathbf{T}_{w2}^{m}\right)^{T} \tag{9}$$

Here, $\mathbf{T}_{w2}^{n}$ is the transformation matrix between the local element and global coordinate systems and $\mathbf{S_V}(x_n, x_m, \omega)$ is the cross-spectral density matrix of turbulence. In generalized coordinates of the still-air and dry mode shapes, the buffeting force spectral matrix will read:

$$\widetilde{\mathbf{S}}_{\mathbf{q}}(\omega) = \mathbf{\Phi}_{aero}^{T}\mathbf{S_{qq}}(\omega)\mathbf{\Phi}_{aero} \tag{10}$$

where $\mathbf{\Phi}_{aero}$ is the mode shape matrix, given at the aerodynamic degrees-of-freedom of the structure.

The self-excited forces acting on the bridge girder and columns are commonly modeled as frequency-dependent aerodynamic stiffness and damping matrices. If the quasi-steady assumption is adopted, the frequency-dependency can be removed and the matrices read:

$$\mathbf{c_{ae}} = \frac{1}{2}\rho UB \begin{bmatrix} 0 & 0 & 0 & 0 & 0 & 0 \\ 0 & -2C_D\left(\frac{D}{B}\right) & C_L - C_D'\left(\frac{D}{B}\right) & 0 & 0 & 0 \\ 0 & -2C_L & -C_L' - C_D\left(\frac{D}{B}\right) & 0 & 0 & 0 \\ 0 & -2C_M & BC_M' & 0 & 0 & 0 \\ 0 & 0 & 0 & 0 & 0 & 0 \\ 0 & 0 & 0 & 0 & 0 & 0 \end{bmatrix},$$

$$\mathbf{k_{ae}} = \frac{1}{2}\rho U^2 B \begin{bmatrix} 0 & 0 & 0 & 0 & 0 & 0 \\ 0 & 0 & 0 & -C_D'\left(\frac{D}{B}\right) & 0 & 0 \\ 0 & 0 & 0 & -C_L' & 0 & 0 \\ 0 & 0 & 0 & BC_M' & 0 & 0 \\ 0 & 0 & 0 & 0 & 0 & 0 \\ 0 & 0 & 0 & 0 & 0 & 0 \end{bmatrix} \tag{11}$$

for a section of the beam element. Alternatively, the matrices can be modeled using the so-called aerodynamic derivatives [51], which can only be obtained using wind tunnel tests. However, for wind speeds concerning buffeting analysis and streamlined box sections such as the BFB section, the quasi-steady assumption gives reasonably accurate estimations. The aerodynamic damping and stiffness matrices can then be obtained for the element degrees of freedom as:

$$\mathbf{C}_{\mathbf{ae}}^{el} = \int_0^L \mathbf{N}^T(x)\mathbf{c_{ae}}\mathbf{N}(x)dx,\ \mathbf{K}_{\mathbf{ae}}^{el} = \int_0^L \mathbf{N}^T(x)\mathbf{k_{ae}}\mathbf{N}(x)dx \tag{12}$$

and then transformed and assembled to the degrees-of-freedom of the FE model, similar to the buffeting forces:

$$\mathbf{C_{ae}} = \sum_{n=1}^{N_{el}} \left(\mathbf{T}_{w2}^n\right)^T \mathbf{C}_{\mathbf{ae}}^n \left(\mathbf{T}_{w2}^n\right),\ \mathbf{K_{ae}} = \sum_{n=1}^{N_{el}} \left(\mathbf{T}_{w2}^n\right)^T \mathbf{K}_{\mathbf{ae}}^n \left(\mathbf{T}_{w2}^n\right) \tag{13}$$

Finally, the matrices in generalized coordinates will read:

$$\widetilde{\mathbf{C}}_{\mathbf{ae}} = \mathbf{\Phi}_{aero}^T \mathbf{C_{ae}} \mathbf{\Phi}_{aero},\ \widetilde{\mathbf{K}}_{\mathbf{ae}} = \mathbf{\Phi}_{aero}^T \mathbf{K_{ae}} \mathbf{\Phi}_{aero} \tag{14}$$

3.4. Stochastic dynamic response

Combining the fluid-structure interaction due to the wind and the waves, the frequency response function of the whole system in generalized coordinates is written as:

$$\widetilde{\mathbf{H}}(\omega) = \left[-\omega^2(\widetilde{\mathbf{M}}_{\mathbf{s}} + \widetilde{\mathbf{M}}_{\mathbf{h}}(\omega)) + i\omega(\widetilde{\mathbf{C}}_{\mathbf{s}} + \widetilde{\mathbf{C}}_{\mathbf{ae}} + \widetilde{\mathbf{C}}_{\mathbf{h}}(\omega)) + (\widetilde{\mathbf{K}}_{\mathbf{s}} + \widetilde{\mathbf{K}}_{\mathbf{ae}}) \right]^{-1} \tag{15}$$

where the cross-spectral density matrix of the combined buffeting and wave loading in generalized coordinates reads:

$$\widetilde{\mathbf{S}}_{\mathbf{tot}}(\omega) = \widetilde{\mathbf{S}}_{\mathbf{p}}(\omega) + \widetilde{\mathbf{S}}_{\mathbf{q}}(\omega) \tag{16}$$

The response of the system in generalized coordinates can then be obtained using the frequency response method:

$$\widetilde{\mathbf{S}}_{\mathbf{r}}(\omega) = \widetilde{\mathbf{H}}^*(\omega)\widetilde{\mathbf{S}}_{\mathbf{tot}}(\omega)\widetilde{\mathbf{H}}(\omega)^T \tag{17}$$

where the asterix denotes the complex conjugate. The displacement response in FE model coordinates can be retrieved using the mode shape matrix:

$$\mathbf{S}_{\mathbf{r}}(\omega) = \mathbf{\Phi}\widetilde{\mathbf{S}}_{\mathbf{r}}(\omega)\mathbf{\Phi}^T \tag{18}$$

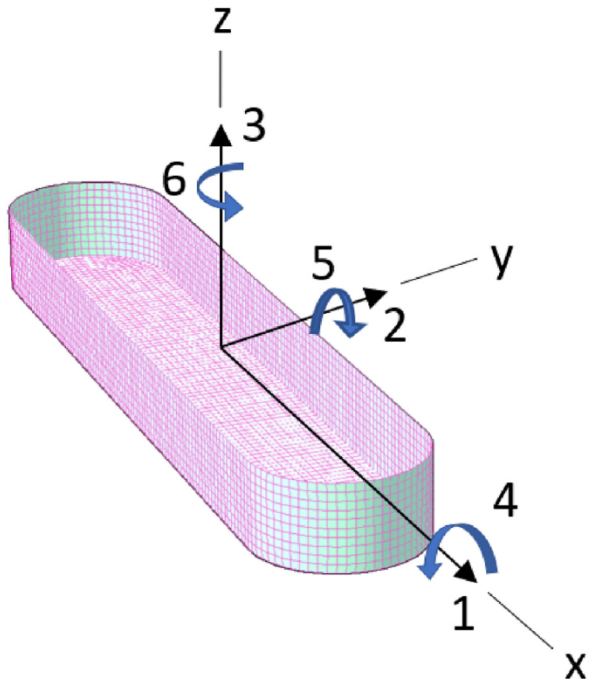

Fig. 8. Panel model of the BFB pontoon P4 in Wadam and the body coordinate system: Degrees-of-freedom from 1 to 6 represent surge, sway, heave, roll, pitch, and yaw motions, respectively.

4. Hydrodynamic interaction of bridge pontoons

Multiple bodies floating in close proximity are known to interact with each other hydrodynamically. This interaction is often a combination of the radiation and the diffraction effects. The wave excitation forces on the bodies will be different due to the altered diffraction wave field because of the presence of the nearby bodies (i.e. changed boundary conditions). Moreover, the radiation forces will also be different since the motion of a body will also induce forces on another body. Such interaction effects can be investigated by model tests, potential flow analyses, or computational fluid dynamics (CFD) simulations. Among these, potential flow theory offers the most practical yet reasonably accurate solution and is therefore widely used.

In the case of the pontoons of the BFB, hydrodynamic interaction effects can also be modeled and the forces on the bodies can be estimated using the potential theory. However, a known problem when using potential theory to model hydrodynamic interaction among multiple bodies is that the theory tends to overestimate the resonant gap responses since it neglects viscous effects. This may consequently result in unrealistically large forces on the bodies at several resonant frequencies. Although this causes an obvious exaggeration of the wave response in very narrow gaps in marine applications (ships in close proximity, side-by-side barges, etc.), the overestimation in the case of the pontoons of a floating bridge is expected to be less severe since the wave energy can still dissipate due to waves propagating outside the computational domain. This is due to the relatively large gap between each pontoon compared to their length. The lack of viscous energy dissipation in the potential flow analyses is commonly overcome by introducing artificial damping to the water surface, which is usually calibrated using model tests. This approach will also be adopted in this study.

4.1. Investigations using potential theory

Two panel-models are used to study the hydrodynamic interaction effects among the BFB pontoons. The first one represents the case neglecting the interaction effects and composed of a single pontoon (P4). The single-pontoon model is shown in Fig. 8. The second model is a multibody model composed of three side-by-side pontoons, modeled as they are in the BFB. Only three pontoons are modeled to reduce the computational complexity and taking advantage of the fact that the pontoons are placed on a circular arch along the bridge. The orientation of the pontoons is shown in Fig. 9 and the coordinates are given in Table 6. It should be noted that any interaction among pontoons that are further than 200 m will be neglected, assuming that the interaction is minor. Furthermore, the models are created in two different solvers, namely Wadam [52] and OrcaWave [53], to verify the results and reduce any software-related bias.

4.2. Artificial damping in potential flow analyses

As introduced at the beginning of the section, the potential theory neglects any viscous effects and tends to overestimate the

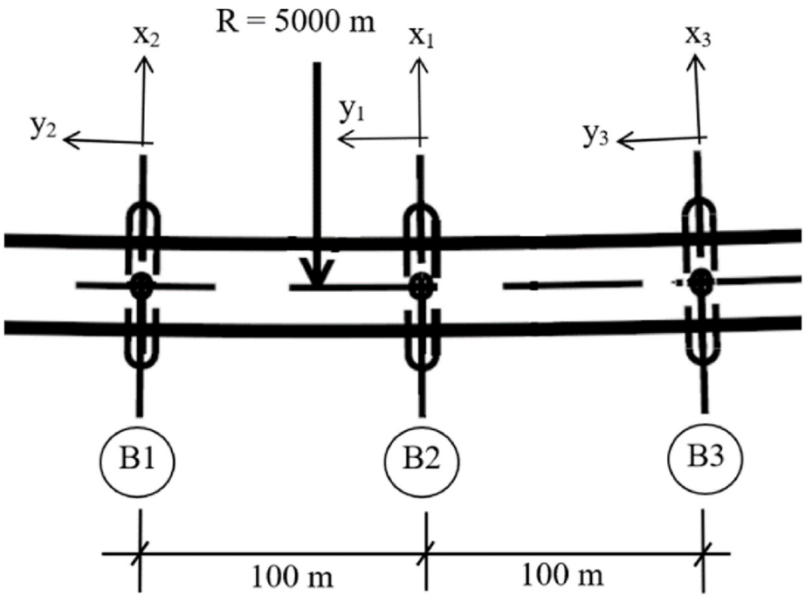

Fig. 9. The 3-pontoon configuration and the body coordinate systems.

Table 6
The 3-pontoon configuration (the coordinates are for the center of gravity of the pontoons in the B2 coordinate system, Rotation-z indicates the orientation of the longitudinal axis of the pontoon).

	x(m)	y(m)	Rotation-z (deg)
B1	1	−100	1.15
B2	0	0	0
B3	1	100	−1.15

resonant gap responses between side-by-side floating bodies. Although this effect is expected to be less severe in the case of the BFB pontoons owing to the relatively large distance between the pontoons, the resonant responses will still be overestimated by a potential theory multibody analysis.

This handicap of the potential flow analyses is often remedied by introducing artificial damping to the flow surface. The conventional linearized free surface condition reads:

$$-\omega^2\varphi_f + g\frac{\partial\varphi_f}{\partial z} = 0 \; on \; z = 0 \tag{19}$$

which represents the non-viscous solution. In the equation, φ_f is the velocity potential and g is the gravitational acceleration. In potential flow solvers, artificial damping can be introduced modifying the free surface condition. Modification of the condition is rather arbitrary and can vary depending on which software is used for analysis. In Wadam, the modified condition is given as:

$$-\omega^2\varphi_f\left(1 - 2i\varepsilon_w - \varepsilon_w^2\right) + g\frac{\partial\varphi_f}{\partial z} = 0 \; on \; z = 0 \tag{20}$$

with the damping coefficient ε_w. The damping coefficient has no direct physical meaning, therefore usually calibrated using data, essentially from model tests or viscous flow simulations. In OrcaWave, the modified free surface condition is given as:

$$-\omega^2\varphi_f(1 - i\varepsilon_o) + g\frac{\partial\varphi_f}{\partial z} = 0 \; on \; z = 0 \tag{21}$$

Given that the damping coefficient is a small number, it is deduced that that $\varepsilon_o = 2\varepsilon_w$, meaning that one should use half of the coefficient used in OrcaWave in their Wadam model to achieve the same amount of damping. Model test data are not yet available for the BFB pontoons considered here. Therefore, it is necessary to use reasonable coefficients recommended in the scientific literature for similar systems. Chen [32] recommends using $\varepsilon_o = 0.016$ for the case of narrow gaps between two barges. Considering also that the damping in our case is likely to be slightly lower due to the larger distance between the bodies, four different damping coefficients are used to conduct the potential flow analyses to observe the sensitivity of the system behavior against the damping coefficient. The coefficients are chosen as 20%, 80%, 100% and 125% of the recommended value $\varepsilon_o = 0.016$. and they are summarized in Table 7.

Table 7
Damping coefficients used in potential flow analyses.

	Chen [32]	20%	80%	125%
Wadam (ε_w)	0.008	0.0016	0.0064	0.01
OrcaWave (ε_o)	0.016	0.0032	0.0128	0.02

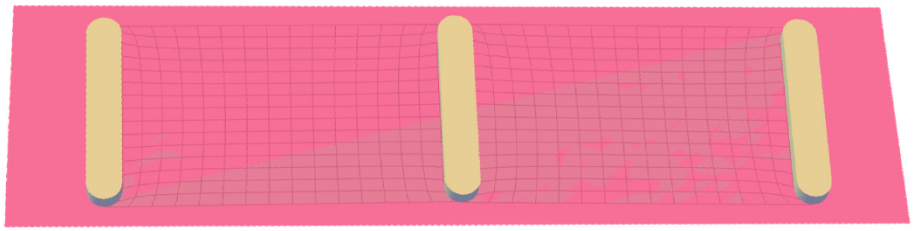

Fig. 10. 3-pontoon multibody model and the damping surface.

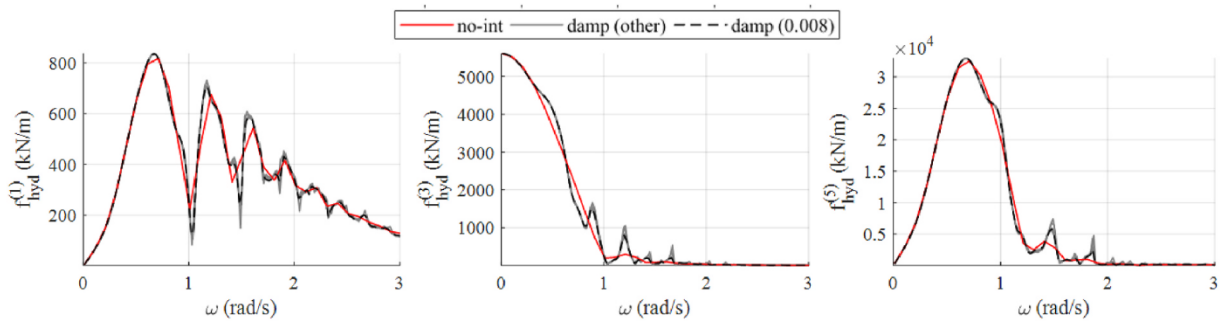

Fig. 11. Wave-excitation transfer functions – 0° Heading – Amplitude (no-int: without interaction effects, damp: with artificial damping).

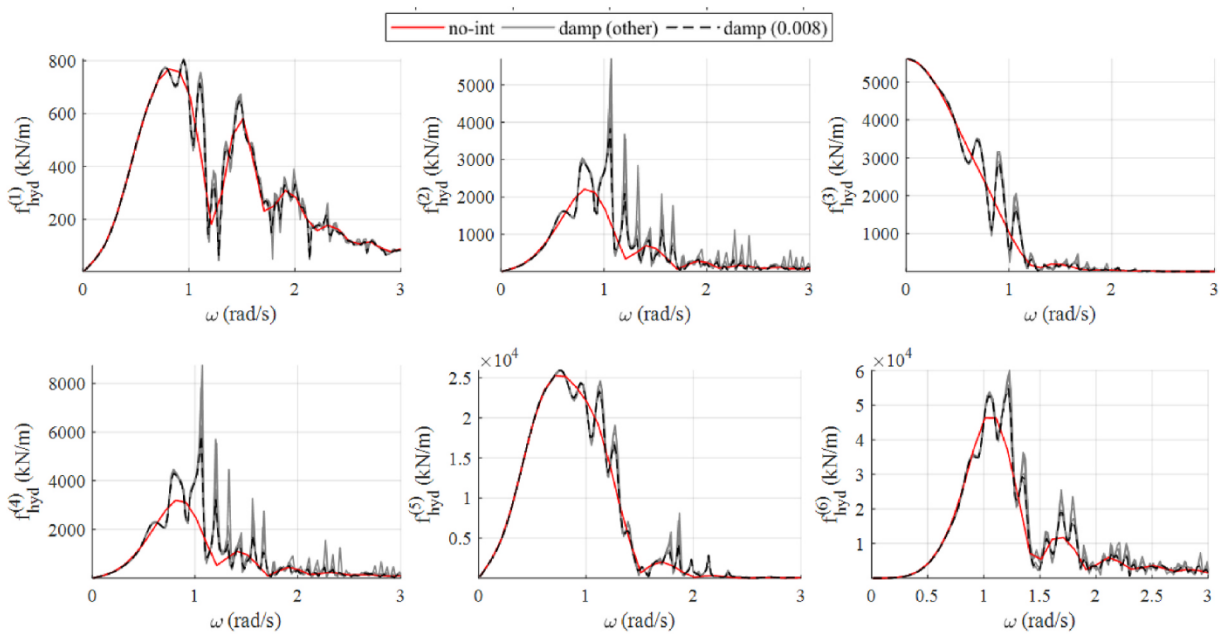

Fig. 12. Wave-excitation transfer functions – 45° Heading – Amplitude (no-int: without interaction effects, damp: with artificial damping).

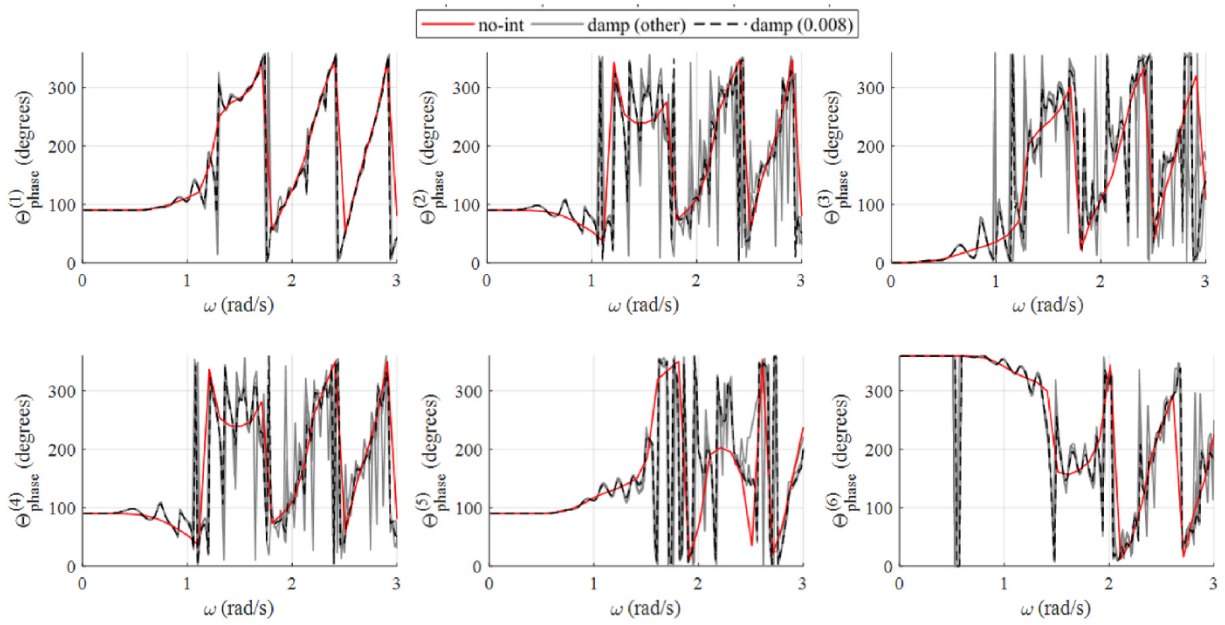

Fig. 13. Wave-excitation transfer functions – 45° Heading – Phase angle (no-int: without interaction effects, damp: with artificial damping).

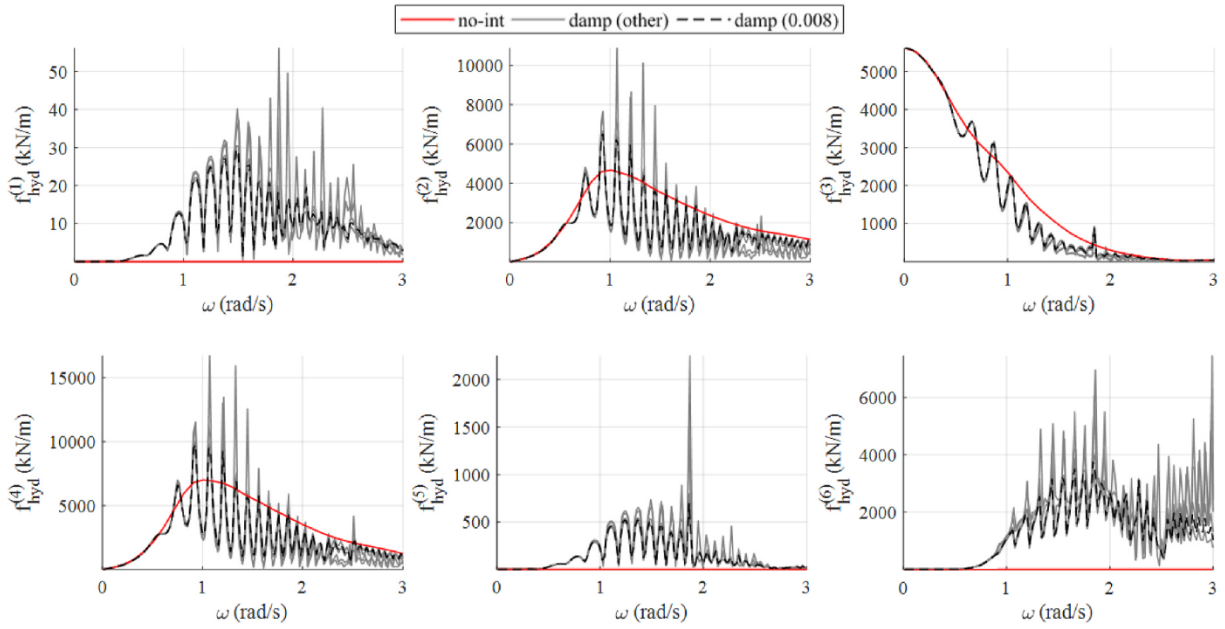

Fig. 14. Wave-excitation transfer functions – 90° Heading – Amplitude (no-int: without interaction effects, damp: with artificial damping).

4.3. Wave excitation transfer functions

According to (2), the calculation of the cross-spectral density matrix of the wave excitation forces on the bridge pontoons requires $\mathbf{\Theta}_n(\omega,\theta)$; the so-called wave excitation transfer functions. These are simply frequency-dependent matrices that describe the forces on the floating body for a unit wave amplitude and they can be obtained using potential flow solvers. For each pontoon, matrices read:

$$\mathbf{\Theta}_n(\omega,\theta) = \left\{\mathbf{f}^{(1)}_{Hyd}(\omega,\theta), \mathbf{f}^{(2)}_{Hyd}(\omega,\theta), \ldots, \mathbf{f}^{(6)}_{Hyd}(\omega,\theta)\right\} \tag{22}$$

where six transfer functions $\mathbf{f}_{Hyd}(\omega,\theta)$ are for the six degrees-of-freedom of the pontoon. In the case where the hydrodynamic inter-

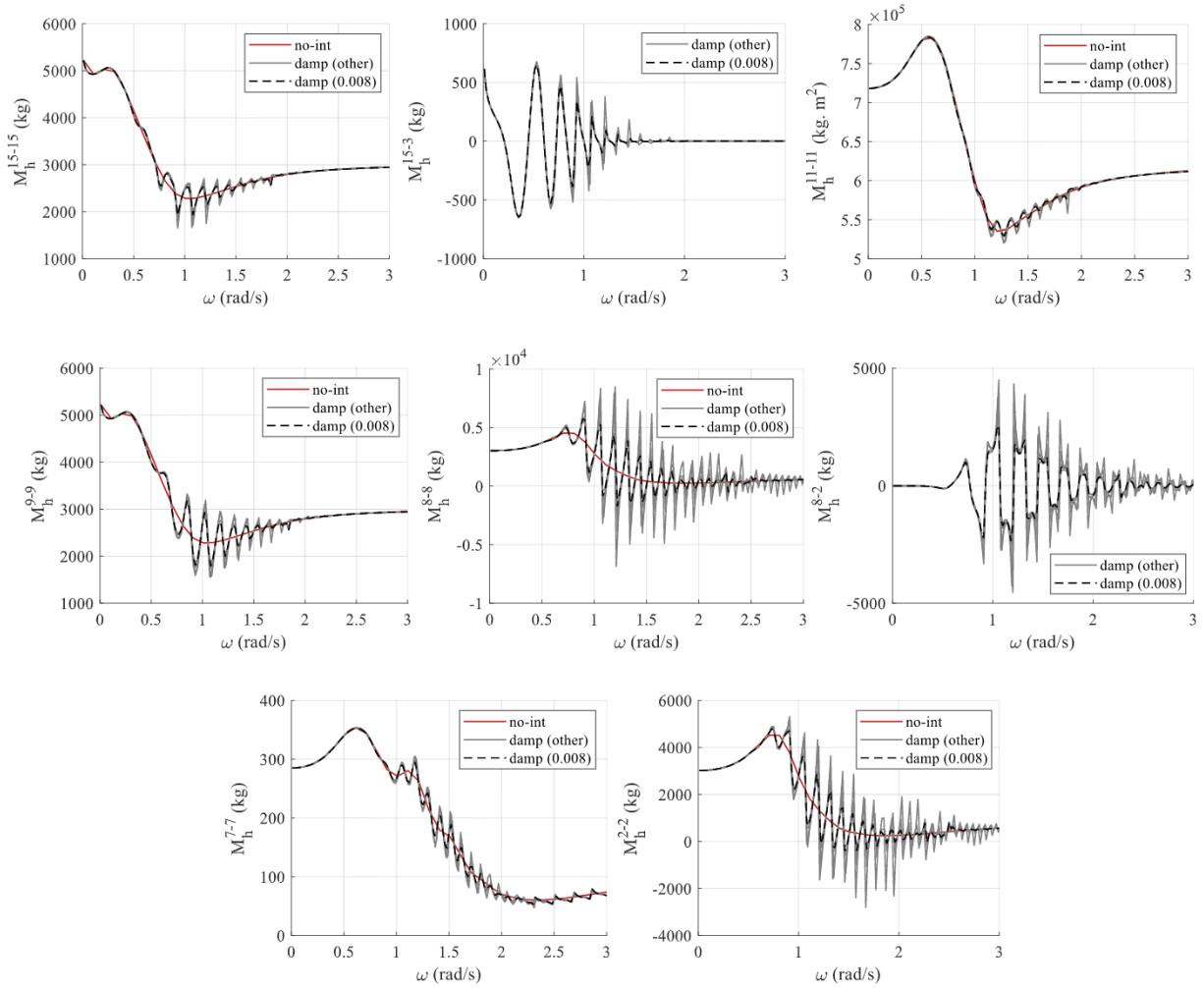

Fig. 15. Added mass coefficients (Degrees-of-freedom 1–6 is of body B1, 7–12 is of B2 and 13–18 is of B3) (no-int: without interaction effects, damp: with artificial damping).

action of the pontoons is neglected, the transfer functions for each pontoon can be obtained using a single-body panel model in a potential flow solver (Fig. 8) for pontoon P4. For the sake of simplicity, only the most common pontoon (P4, Table 1) is modeled. The amplitude of the transfer functions for the pontoon are presented through Figs. 11–14 for different heading angles. For the 45° heading, the phase angles of the transfer functions are also presented as an example.

Following the same methodology, multibody analyses are also conducted using the multibody panel model shown in Fig. 10. Three floating pontoons are modeled and artificial damping is applied to the water surface between the bodies. Similar to the case of the single-pontoon model, the transfer functions are obtained for each body. The difference is that the resulting transfer functions account for the changed diffraction wave field due to the presence of the adjacent pontoons. The resulting transfer functions are presented in figures through Figs 11–14 for different damping coefficients along with the single-pontoon case. The degrees-of-freedom with negligible forces are omitted from the figures. The degrees-of-freedom for a body are defined earlier in Fig. 8. It should be noted that the results presented here are obtained by Wadam, but replicated with very good agreement in OrcaWave. Only Wadam results are plotted for brevity.

The results show some peaks in the force transfer functions due to the resonant motion of the fluid between the bodies. The increase in forces in the case of 0° heading angle (waves perpendicular to the pontoon x-axis) is visible but small. However, when the waves become more skewed (45–90° heading angle), it is seen that many resonant peaks are seen and the forces at peaks may be significantly larger compared to the single pontoon case. This is especially the case for the lateral force and the torsional moment for 45°. In the case of beam sea (90° approach angle), a shielding effect (reduced forces on a body due to shielding from another body) can also be observed in degrees-of-freedom 2,3 and 4, where the average of the peaked curves lies below the curve of the single-pontoon case.

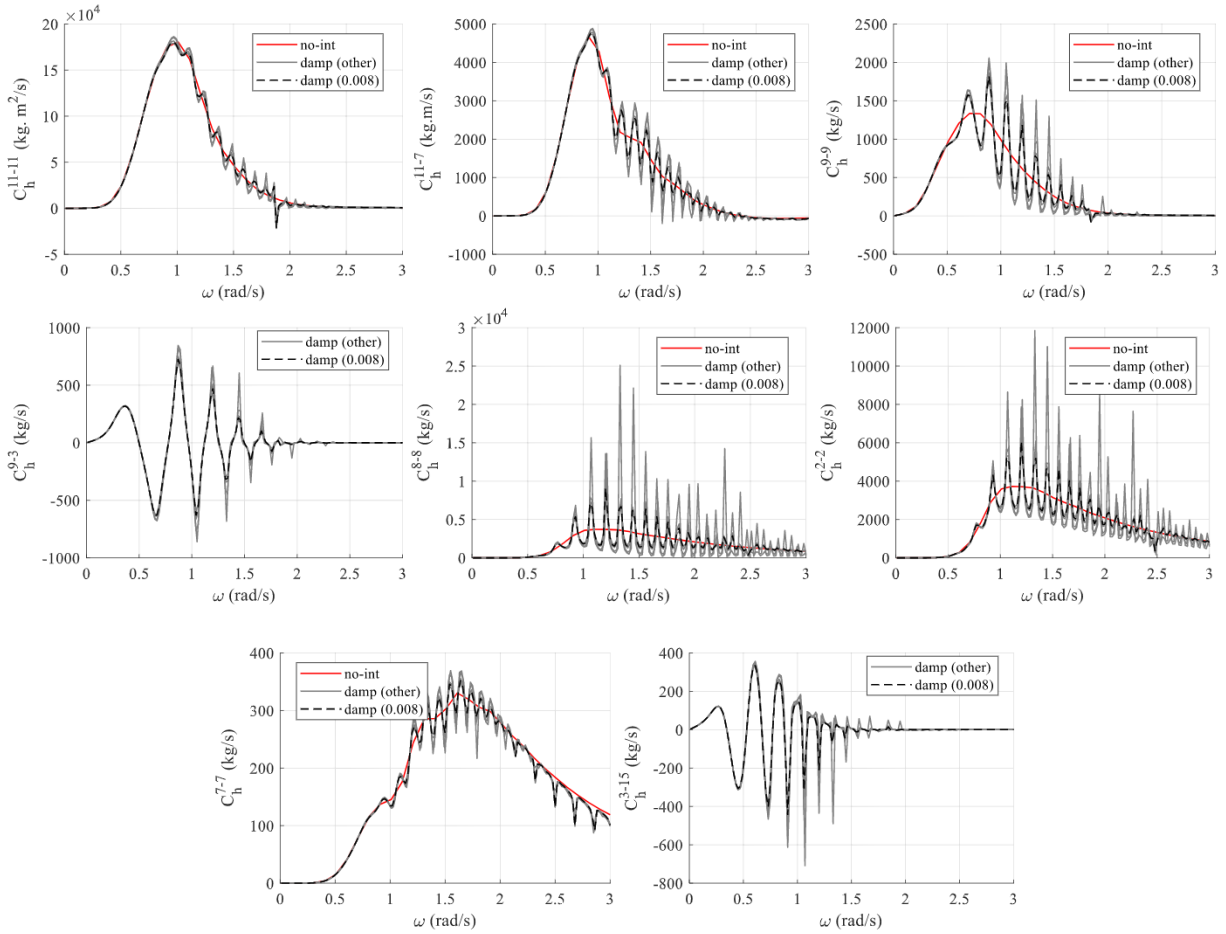

Fig. 16. Potential damping coefficients (Degrees-of-freedom 1–6 is of body B1, 7–12 is of B2 and 13–18 is of B3) (no-int: without interaction effects, damp: with artificial damping).

4.4. Added mass & potential damping

If a single pontoon is modeled in the potential flow solver, the added mass and potential damping terms are obtained by forcing a unit motion in one degree-of-freedom and solving for the forces in all degrees-of-freedom. This results in 6×6 matrices for the floating body. Alternatively, if a multibody model is adopted composed of 3 bodies as in Fig. 9, there will be additional terms due to interaction among bodies. For instance, the motion of body B1 shown in Fig. 9 will induce forces on the other bodies B2 and B3. Furthermore, the forces on a body due to its own motion will be altered because of the presence of the other bodies. The resulting added mass and potential damping matrices for a certain frequency will then be 18×18 matrices for 3 bodies.

Some important added mass and potential damping terms are presented in Figs. 15 and 16 for the 3-pontoon configuration given in Fig. 9. The relative importance of the terms are determined by sensitivity analyses. The terms that cause the largest impact on the global responses are chosen to be presented. However, in total, there are 324 terms for both matrices and the matrices are symmetric. The results are given for different artificial damping coefficients and the single-pontoon term (no-interaction) is plotted along with the results if relevant. Many resonant peaks can be observed in both the added mass and the potential damping terms, especially between 1 and 2 rad/s. The peaks are especially pronounced in the case of lateral and vertical motions and forces.

5. Implementation of hydrodynamic interaction effects in the frequency domain framework

Having obtained the wave-excitation transfer functions and the added mass and potential damping matrices from potential flow analyses, we need to integrate the interaction effects to the framework described in Section 2 to predict the bridge response.

For the case of the wave-excitation transfer functions, the assembly is quite straightforward, as $\mathbf{\Theta}_n(\omega,\theta)$ matrices for each pontoon will be replaced by the ones obtained from the multibody analysis with three pontoons. For the end pontoons, $\mathbf{\Theta}_{B1}(\omega,\theta)$ and $\mathbf{\Theta}_{B3}(\omega,\theta)$ will be used for the bodies B1 and B3 shown in Fig. 9. The remaining pontoons will be assembled using $\mathbf{\Theta}_{B2}(\omega,\theta)$, which represents the case with pontoons on both sides. Both the coordinate transformations and the assembly follow the same procedure highlighted earlier.

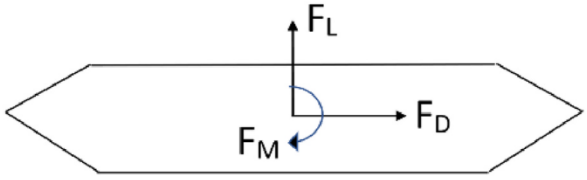

Fig. 17. Aerodynamic forces acting on a bridge section.

If the hydrodynamic interaction among the pontoons is neglected, the added mass and potential damping matrices of the bridge can be assembled using (5), after transforming each matrix to global coordinates. More explicitly, the system matrices will look like:

$$\mathbf{M_h} = \begin{bmatrix} \mathbf{T}_1^T\mathbf{M}_h\mathbf{T}_1 & & & \mathbf{0} \\ & \mathbf{T}_2^T\mathbf{M}_h\mathbf{T}_2 & & \\ & & \ddots & \\ \mathbf{0} & & & \mathbf{T}_n^T\mathbf{M}_h\mathbf{T}_n \end{bmatrix} \tag{23}$$

where $\mathbf{T}_n$ is the local to global transformation matrix for pontoon n. Only added mass is written as potential damping follows the same rules. If the hydrodynamic interaction effects are accounted for; however, additional terms will have to be introduced since the pontoons in close proximity (~200 m) will interact with each other. This will result in a banded matrix which can be assembled as below:

$$\mathbf{M_h} = \begin{bmatrix} \mathbf{T}_1^T\mathbf{M}_h^{11}\mathbf{T}_1 & \mathbf{T}_1^T\mathbf{M}_h^{12}\mathbf{T}_2 & \mathbf{T}_1^T\mathbf{M}_h^{13}\mathbf{T}_3 & & & & & \\ \mathbf{T}_2^T\mathbf{M}_h^{21}\mathbf{T}_1 & \mathbf{T}_2^T\mathbf{M}_h^{22}\mathbf{T}_2 & \mathbf{T}_2^T\mathbf{M}_h^{23}\mathbf{T}_3 & \mathbf{T}_2^T\mathbf{M}_h^{13}\mathbf{T}_4 & & & & \\ \mathbf{T}_3^T\mathbf{M}_h^{31}\mathbf{T}_1 & \mathbf{T}_3^T\mathbf{M}_h^{32}\mathbf{T}_2 & \mathbf{T}_3^T\mathbf{M}_h^{22}\mathbf{T}_3 & \ddots & \ddots & & & \\ & \mathbf{T}_4^T\mathbf{M}_h^{31}\mathbf{T}_2 & \ddots & \ddots & \ddots & \mathbf{T}_{n-3}^T\mathbf{M}_h^{13}\mathbf{T}_{m-1} & & \\ & & \ddots & \ddots & \mathbf{T}_{n-2}^T\mathbf{M}_h^{22}\mathbf{T}_{m-2} & \mathbf{T}_{n-2}^T\mathbf{M}_h^{23}\mathbf{T}_{m-1} & \mathbf{T}_{n-2}^T\mathbf{M}_h^{13}\mathbf{T}_m & \\ & & & \mathbf{T}_{n-1}^T\mathbf{M}_h^{31}\mathbf{T}_{m-3} & \mathbf{T}_{n-1}^T\mathbf{M}_h^{32}\mathbf{T}_{m-2} & \mathbf{T}_{n-1}^T\mathbf{M}_h^{22}\mathbf{T}_{m-1} & \mathbf{T}_{n-1}^T\mathbf{M}_h^{23}\mathbf{T}_m & \\ & & & & \mathbf{T}_n^T\mathbf{M}_h^{31}\mathbf{T}_{m-2} & \mathbf{T}_n^T\mathbf{M}_h^{32}\mathbf{T}_{m-1} & \mathbf{T}_n^T\mathbf{M}_h^{33}\mathbf{T}_m & \end{bmatrix} \tag{24}$$

where $\mathbf{M}_h^{ij}$, $i = \{1,2,3\}$, $j = \{1,2,3\}$ are the matrices obtained from the multi-body potential flow analyses. The potential damping will not be repeated as it is similar. The transformation to the generalized coordinates will follow the same procedure as given earlier in Eqn. (6).

6. Global analyses

6.1. Modeling of the environmental loads

The purpose of the study is to investigate the effects of the hydrodynamic interaction among the bridge pontoons on the global responses. Therefore, we seek a realistic representation of the extreme environmental loading on the structure to observe the effects of hydrodynamic interaction on the bridge response. The wind and the wave conditions are therefore modeled based on the design basis documents prepared by the Norwegian Public Roads Administration (NPRA) for the recent design stages of the bridge [54]. The environmental conditions were obtained using a combination of site measurements and hindcast simulation data. The Weather Research Forecasting (WRF) model [55] was used for the hindcast simulations of the mean wind conditions, where SWAN (TU Delft [56], was used to model the wave conditions. The wind measurements were taken using anemometers on meteorological masts near the bridge site and the wave heights and directions in the fjord were measured using Datawell Waverider buoys. A common averaging period of 1 h is used for obtaining the wind and wave statistics, an interval where both processes are assumed to be reasonably stationary.

6.1.1. Wind loads

The dynamic wind loads on the bridge are comprised of the buffeting loading due to the incident turbulence in the wind and the self-exited forces which arise due to the fluid-structure interaction. For the analyses here, we will consider the dynamic wind loading on the main girder and the pontoon columns. The wind actions on the cables of the high-bridge at the south end of the bridge will be neglected as their impact is insignificant for our application. The formulation of the self-excited forces is given in Eqn. (11) and the buffeting forces are given in Eqn. (7) under the quasi-steady assumption. Both formulations require the static force coefficients of the girder. These are defined as:

Table 8
Steady-state aerodynamic coefficients of the BFB deck section.

C_D	C_L	C_M	C_D'	C_L'	C_M'
0.95	−0.629	−0.076	−2.33	3.59	1.105

$$C_D = \frac{F_D}{0.5\rho U^2 D},\ C_L = \frac{F_L}{0.5\rho U^2 B},\ C_M = \frac{F_M}{0.5\rho U^2 B^2} \tag{25}$$

where F_D, F_L, F_M are the aerodynamic forces acting on the section as shown in Fig. 17. The coefficients for the BFB deck were obtained through wind tunnel tests by Ref. [57] and given in Table 8. The drag coefficient of the pontoon columns is taken as 0.8. The derivatives of the coefficients were estimated against the angle-of-attack in the range (−3°,3°).

The mean wind speed with a return period of 100 years at a reference height of 10 m from sea level is given as $U_{10} = 25.2$ m/s for the easterly winds by the design basis. The vertical profile of the mean wind speed is given as the following logarithmic profile:

$$U_z = U_{10}\frac{\ln(z/z_0)}{\ln(10/z_0)} \tag{26}$$

where z_0 is the roughness length, which is taken as 0.01. U_z denotes the wind speed at height z.

The calculation of the buffeting loading on the bridge hinges on the cross-spectral density matrix of the turbulence (Eqn. (9)), which reads:

$$S_V(\mathbf{s}_{nm},\omega) = \begin{bmatrix} S_u(\omega)C_u(\mathbf{s}_{nm},\omega) & & \\ & S_v(\omega)C_v(\mathbf{s}_{nm},\omega) & \\ & & S_w(\omega)C_w(\mathbf{s}_{nm},\omega) \end{bmatrix} \tag{27}$$

where

$$\mathbf{s}_{nm} = \{\Delta x, \Delta y, \Delta z\},\ \Delta x = |x_n - x_m| \tag{28}$$

if the cross-spectral terms between turbulence components are neglected. $S_i(\omega),\ i \in \{u,v,w\}$ are the one point spectra of turbulence for the three turbulence components: along-wind component (u), across-wind component (v), and vertical component (w). The one point-spectra are modeled using the N400 guidelines [58] for bridge design in Norway as

$$\frac{\omega S_i(\omega)}{\sigma_i^2} = \frac{A_i\widehat{\omega}_i}{(1+1.5A_i\widehat{\omega}_i)^{5/3}},\ \widehat{\omega}_i = \frac{\omega L_i(z)}{U(z)},\ i \in \{u,v,w\} \tag{29}$$

where σi are the standard deviations of the turbulence components. The turbulence intensities are related to σi and can be written as below:

$$I_i = \frac{\sigma_i}{U(z)},\ I_u = 0.112,\ \begin{bmatrix} I_v \\ I_w \end{bmatrix} = \begin{bmatrix} 0.84 \\ 0.6 \end{bmatrix} I_u \tag{30}$$

according to the site measurements. The spectral parameters Ai and the integral length scales Li are taken from the N400 recommendations and shown in Table 9. As apparent from Eqn. (27), the calculation of the cross-spectral density matrix also requires the coherence (normalized cross-spectral density) terms, which can be modeled using Davenport's formula as

$$C_i\left(\mathbf{s},\omega\right) = \exp\left(-K_{eq,i}\frac{\omega}{U(z)}\right),\ K_{eq,i} = \sqrt{(K_{ix}\Delta x)^2 + \left(K_{iy}\Delta y\right)^2 + (K_{iz}\Delta z)^2} \tag{31}$$

The parameters $K_{ix}, K_{iy}, K_{iz}\ i \in \{u,v,w\}$ are called decay coefficients of turbulence parameters where $\{x,y,z\}$ define a cartesian coordinate system of the turbulence components. Therefore, K_{uz} for instance, denotes the decay coefficient of the along-wind

Table 9
Turbulence parameters.

I_i (%)	11.2	9.4	6.7
$A_i/(2\pi)$	6.8	9.4	9.4
L_i (m)	162	12.5	4.2
$K_{ix}(2\pi)$	0	0	0
$K_{iy}(2\pi)$	10	6.5	6.5
$K_{iz}(2\pi)$	10	6.5	3

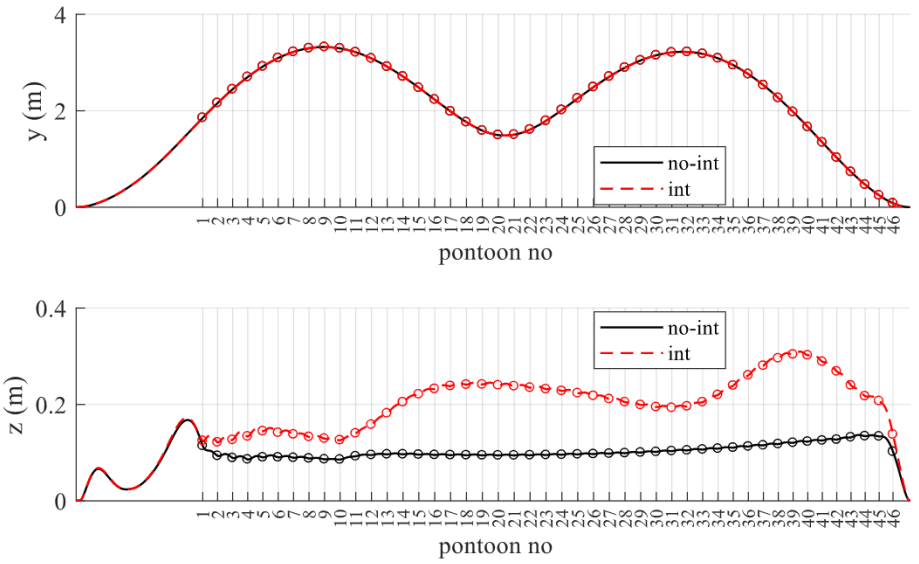

Fig. 18. RMS displacement responses of the bridge girder in global coordinates (z: vertical, y: transverse displacement). The pontoon locations are indicated by circular markers. (int: interaction effects included, no-int: interaction effects not included).

turbulence in the vertical direction. The decay coefficients used are shown in Table 9, which are taken from N400 [58] but in very reasonable agreement with the site data in the average sense.

6.1.2. Wave loads

Similar to the case of the wind loads, the calculation of the cross-spectral density matrix of the wave elevation (Eqn. (3)) requires the one-dimensional wave spectrum $S_\eta(\omega)$ and the directional spectrum $D(\theta)$. Here, the one-dimensional wave spectrum is modeled using the JONSWAP spectrum as:

$$S(\omega) = \frac{5H_s\omega_p^4(1-0.278\ln(\gamma))}{16\omega_p}\exp\left(-1.25\frac{\omega_p^4}{\omega^4}\right)\gamma^{\exp\left(\frac{(\omega-\omega_p)^2}{2\sigma^2\omega_p^2}\right)}$$
$$\sigma = \left\{\begin{matrix}0.07\ for\ \omega \le \omega_p\\ 0.09\ for\ \omega > \omega_p\end{matrix}\right\},\ \omega_p = 2\pi \Big/ T_p \tag{32}$$

where H_s and T_p denote the significant wave height and the peak period, respectively. The directional distribution is modeled using the cos-2s distribution with the parameter s = 3 and the mean wave direction is assumed perpendicular to the bridge and approaching from the East. Environmental contour analyses of the wave conditions in the fjord gave a 100-year sea state with $H_s = 2.1$ m and $T_p = 5.5$ s for the waves coming from the East. The second-order waves are neglected owing to the preliminary investigation results [59,60] which revealed that the low-frequency response of the bridge was dominated by the wind actions. Although they might affect the mean responses slightly, their effect on the dynamic response was found negligible. The hydrodynamic interaction effects in second-order wave loads, however, will be addressed in future studies and considered out-of-scope of this paper.

6.2. Analysis results

6.2.1. Displacements and section forces of the girder

Stochastic dynamic analyses of the bridge under combined wind and wave loading were performed in the frequency domain with the framework and the environmental conditions described in the previous sections. The analyses were conducted initially without the hydrodynamic interaction effects and repeated after including the interaction. In the case where the interaction is modeled, the artificial damping coefficient is taken as 0.008 in Wadam (Table 7), i.e. the recommendation by Chen [32]. The displacement spectra of the girder were obtained by transforming the spectra of generalized response into the global coordinate system of the FE model using the mode shape matrix. The root-mean-square (RMS) response of the girder was then obtained by integrating the auto-spectra of the response for each degree-of-freedom over the entire frequency range (0–3 rad/s). The RMS displacement responses obtained for the transverse and vertical motions of the girder are shown in Fig. 18 for both with and without the effects of hydrodynamic interaction. A significant and asymmetrical increase is observed in the vertical response when the interaction effects are modeled.

The section forces at the girder were obtained in a similar manner by transforming the generalized response spectra using the mode shape matrix of the section forces. The integrated RMS responses are shown in Fig. 19. Significant increases are observed in the axial

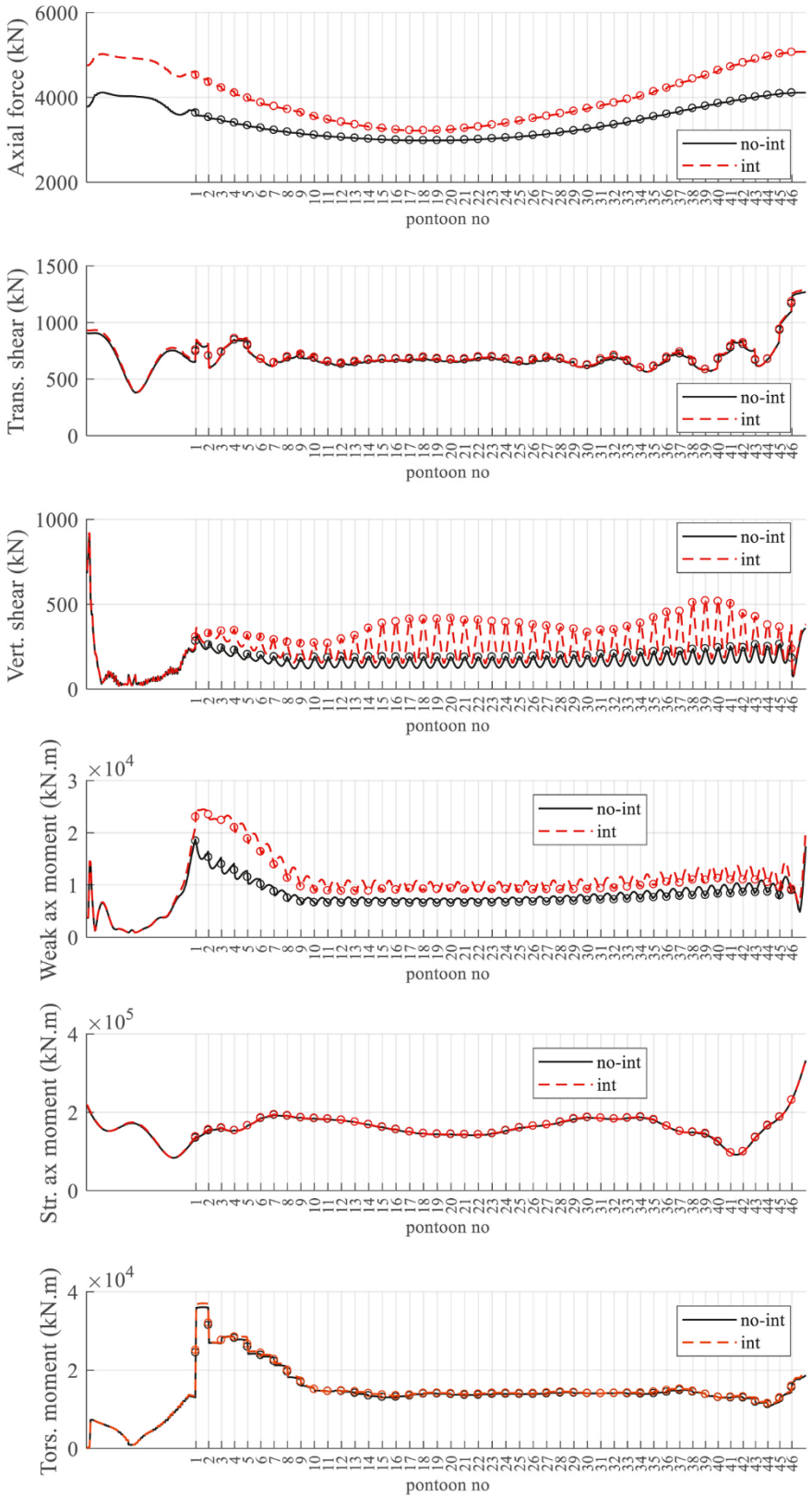

Fig. 19. RMS section forces of the bridge girder. The pontoon locations are indicated by circular markers. (trans: transverse, weak ax.: weak-axis, str. ax.: strong-axis, tors.: torsional) (int: interaction effects included, no-int: interaction effects not included).

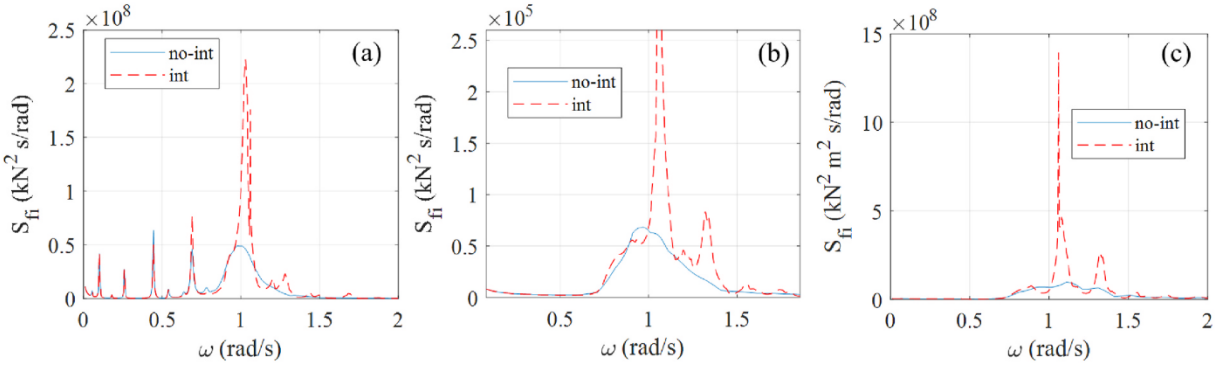

Fig. 20. Auto-spectral densities of the section forces at the girder – the cases with and without hydrodynamic interaction: a) Axial force at x = 0.1 m. b) vertical shear at x = 2645 m. c) Weak-axis bending moment at x = 1007 m. (int: interaction effects included, no-int: interaction effects not included).

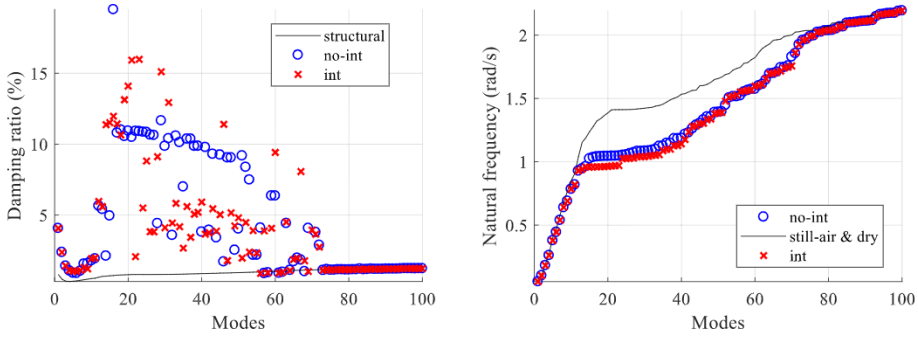

Fig. 21. Modified dynamic properties of the bridge due to fluid-structure interaction. The plots show the cases with and without hydrodynamic interaction of the pontoons. Modal damping ratios (on the left) and Natural frequencies (on the right) (int: interaction effects included, no-int: interaction effects not included).

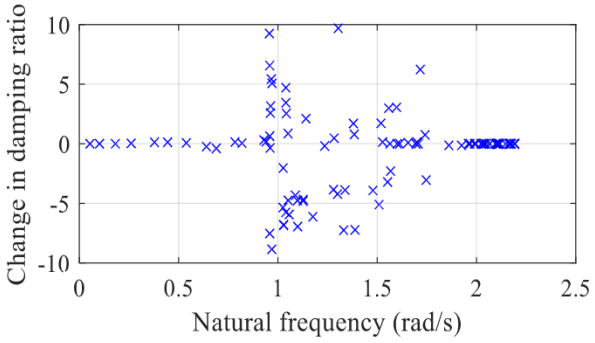

Fig. 22. Change in modal damping ratio. Positive values indicate an increase in the damping ratio when the hydrodynamic interaction effects are included.

force (at most 25%), vertical shear force (at most 126%), and the weak axis bending moment (at most 89%) of the girder. The maximum increase in the axial force occurred at the ends of the girder, near the supports. In the case of the vertical shear, the maximum increase occurred near the midspan, where it was concentrated around the pontoons near the high bridge for the weak axis moment. The auto-spectra of these three response quantities are given in Fig. 20 at the girder positions where the most difference is observed. The spectral densities show that the wind-induced response is essentially not affected by the hydrodynamic interaction as it is in the low-frequency range. The wave-induced response, on the other hand, seems to be largely affected by the interaction. Although the wide-banded response observed in the case without interaction remained almost the same, large peaks were introduced by the interaction at several frequencies, indicating resonant effects. The peaks are apparent in all three response components around the same frequencies (1.05 rad/s, 1.32 rad/s).

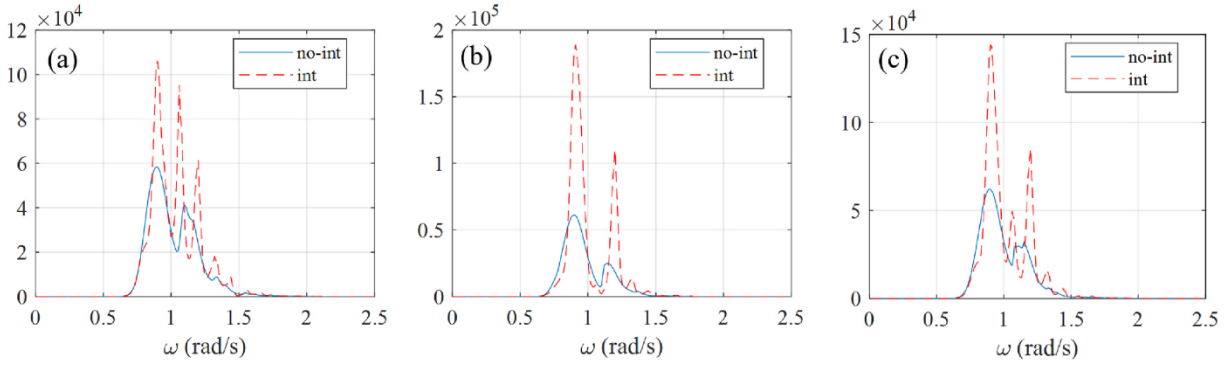

Fig. 23. Auto-spectral densities of the generalized wave force – the cases with and without hydrodynamic interaction: a) mode 20 (1.38 rad/s) b) mode 25 (1.41 rad/s) c) mode 33 (1.44 rad/s). Note that the mode numbers refer to the still-air & dry vibration modes of the structure. (int: interaction effects included, no-int: interaction effects not included).

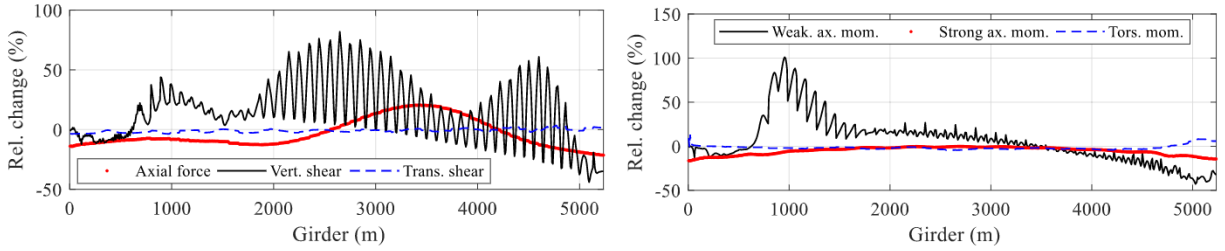

Fig. 24. Mean wave direction SE: Relative change in RMS section forces when hydrodynamic interaction is accounted for. Section forces on the left and moments on the right.

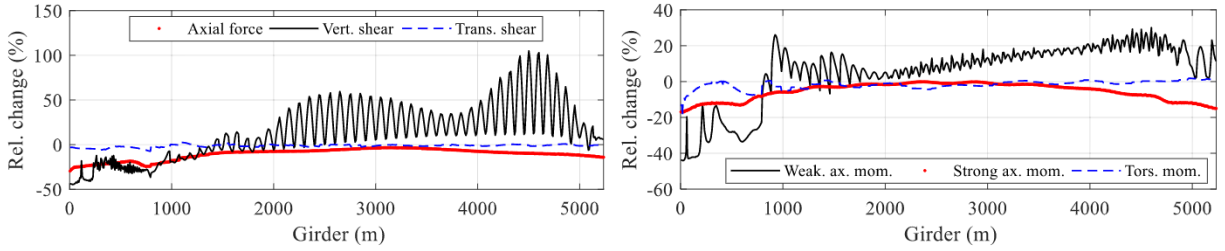

Fig. 25. Mean wave direction NE: Relative change in RMS section forces when hydrodynamic interaction is accounted for. Section forces on the left and moments on the right.

6.2.2. Modal analysis

Dynamic properties of the structure, namely its natural frequencies and modal damping ratios were identified to get further insight into the nature of hydrodynamic interaction effects. The dynamic properties of the bridge change under the combined wind and wave loading, due to the fluid-structure interaction. As the system matrices representing the radiation and the self-excited forces are frequency-dependent, the modal analysis was carried out in an iterative manner [2]. The resulting modal damping ratios and the corresponding natural frequencies are presented in Fig. 21. It is seen that in the low-frequency range most of the damping is due to aerodynamic damping, which is not affected by the hydrodynamic interaction as interaction effects are minor in this frequency range. It should also be mentioned that drag damping, although neglected here, may provide additional damping to the system in this frequency range. Between modes 20 and 60, however, the hydrodynamic damping dominates. Here, relatively large differences between the modal damping ratios are observed when hydrodynamic interaction is accounted for. These differences are shown more clearly in Fig. 22. It should be noticed that the damping is reduced significantly at the frequency range where we observed the increase in the spectral responses (Fig. 20). The reduced damping combined with the increase in the wave forces at the frequency range in question explains the observed increase in the response quantities. The auto-spectral densities of the generalized wave force are given in Fig. 23 for several dry modes of the structure. It is seen that several peaks are introduced to the spectra due to the hydrodynamic interaction of the pontoons.

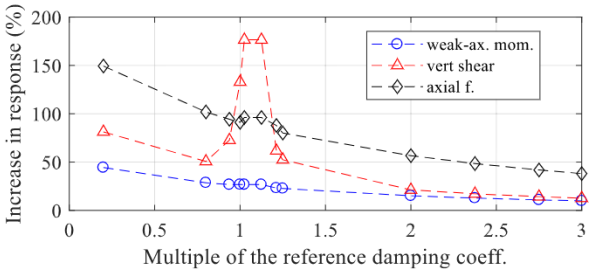

Fig. 26. The increase in responses (load effects) due to hydrodynamic interaction as a function of the damping coefficient (reference damping coefficient refers to $\zeta_w = 0.008$).

6.2.3. *Wave direction*

The initial analyses are carried out assuming a mean wave direction that is perpendicular to the x-axis shown in Fig. 3, which almost coincides with the East, and is referred to as such here (i.e. waves from the East). However, the hydrodynamic interaction effects on the wave loading depend highly on the wave direction, as can be observed from Fig. 11–14. Therefore, further analyses are carried out to reveal the sensitivity of the results to the incoming wave direction. The analyses described earlier are repeated using two additional mean wave directions deviating 45° from the perpendicular direction. These will be referred to as Northeast (NE) and Southeast (SE) directions. For the two directions, the differences in RMS section forces between the cases with and without hydrodynamic interaction are shown in Fig. 24 and Fig. 25 for the SE and NE direction, respectively. For the SE direction, the changes in the weak-axis bending moment and the axial force are particularly noteworthy for the bridge response. The vertical shear force also increases significantly, also for the NE direction; however, it should be mentioned that its contribution to the design stresses is relatively small [57]. Therefore, it can be concluded that the case of the SE waves is more critical in terms of hydrodynamic interaction.

6.2.4. *Artificial damping*

The increases in the load effects are also dependent on the damping coefficient chosen in the potential flow solutions. The uncertainty in this parameter is inevitable unless the coefficient is calibrated using reliable experimental data. Therefore, it is deemed necessary to show the effect of the parameter on the load effects in question. The damping coefficient was therefore altered greatly and the analyses were repeated for several values of the damping coefficient. The results are shown in Fig. 26. It is apparent that the change in load effects decreases in general as the damping coefficient increases, which is an expected result. An exception of this is observed in the case of the vertical shear force, where a peak in the response is visible for a particular damping range. This occurs due to resonance of a vertical mode due to very low damping at that vibration mode, which in turn gives drastic increases in the shear force due to the nature of the mode. Such counter intuitive behavior once again demonsrates the complexity of the dynamic phenomenon that is dealt with. As can be seen in Fig. 16, the inter-pontoon potential damping terms can be negative, which might cause the total damping to be critically low, or even negative. Still, even with drastic increases in the coefficient, we observe increased responses when hydrodynamic interaction is included. Moreover, the system becomes less sensitive to the damping coefficient when the coefficient is large.

The proposed analysis methodology provides practical means for assessment of hydrodynamic interaction effects on floating bridges. The next step is the verification of the methodology by comparison with test results. Such tests in the ocean basin are already undertaken by SINTEF and research will continue toward verification of the simulation results.

7. Conclusions

The effect of hydrodynamic interaction of the bridge pontoons on the dynamic section responses of a floating bridge is investigated numerically using state-of-the-art potential flow simulations combined with stochastic dynamic analyses in the frequency domain. Several important conclusions can be drawn from the study concerning the design of floating pontoon bridges against dynamic wind and wave actions.

- Multibody potential flow analyses of the bridge pontoons revealed a significant interaction between bodies, which imposed resonant peaks on both the radiation and the wave-excitation forces.
- In the case study considered here, increases in the axial force and the weak-axis bending moment of the girder are observed due to a combination of reduced hydrodynamic damping and resonant amplification in the wave excitation forces.
- The findings suggest that the hydrodynamic interaction of the pontoons should be considered in the design stage of such structures, as it can cause an increase in the design stresses.
- The framework presented here will be useful in a design situation as it provides means for rapid assessment of the phenomenon. For instance, using such an approach, the interaction effects can be minimized by altering the design, e.g. by varying the distance between the pontoons or their orientation.

Declaration of competing interest

The authors declare that they have no known competing financial interests or personal relationships that could have appeared to influence the work reported in this paper.

Acknowledgments

The research described here was financed by the Norwegian Public Roads Administration through the E39 Coastal Highway Project.

References

[1] Kvåle KA. Dynamic behaviour of floating bridges exposed to wave excitation A numerical and experimental investigation. NTNU; 2017.
[2] Kvåle KA, Sigbjörnsson R, Øiseth O. Modelling the stochastic dynamic behaviour of a pontoon bridge: a case study. Comput Struct 2016;165:123–35. https://doi.org/10.1016/j.compstruc.2015.12.009.
[3] Moe G. Design philosophy of floating bridges with emphasis on ways to ensure long life. J Mar Sci Technol 1997.
[4] Wang CM, Watanabe E, Utsunomiya T. Very large floating structures: applications, analysis and design. Tailor & Fransis; 2008.
[5] Watanabe E. Floating bridges: past and present. Struct. Eng. Int. J. Int. Assoc. Bridg. Struct. Eng. 2003. https://doi.org/10.2749/101686603777964810.
[6] Kvåle KA, Øiseth O. Structural monitoring of an end-supported pontoon bridge. Mar Struct 2017;52:188–207. https://doi.org/10.1016/j.marstruc.2016.12.004.
[7] Cheng Z, Gao Z, Moan T. Hydrodynamic load modeling and analysis of a floating bridge in homogeneous wave conditions. Mar Struct 2018. https://doi.org/10.1016/j.marstruc.2018.01.007.
[8] Fenerci A, Xu Y, Øiseth O. Numerical studies on the dynamic behavior of a super-long curved pontoon bridge under wind and wave actions. In: COMPDYN proceedings; 2019. https://doi.org/10.7712/120119.7352.19214.
[9] Fu S, Ou S, Deng S, Wei W, Moan T, Lie H. A time-domain method for hydroelastic analysis of floating bridges in inhomogeneous waves. In: Proceedings of the international conference on offshore mechanics and arctic engineering - omae; 2017. https://doi.org/10.1115/OMAE2017-62534.
[10] Seif MS, Inoue Y. Dynamic analysis of floating bridges. Mar Struct 1998;11:29–46. https://doi.org/10.1016/S0951-8339(97)00012-9.
[11] Xu Y, Øiseth O, Moan T. Time domain simulations of wind- and wave-induced load effects on a three-span suspension bridge with two floating pylons. Mar Struct 2018. https://doi.org/10.1016/j.marstruc.2017.11.012.
[12] Holand I, Sigbjörnsson R, Langen I. Dynamic analysis of a curved floating bridge. IABSE Proceedings 1977.
[13] Langen I, Sigbjörnsson R. On stochastic dynamics of floating bridges. Eng Struct 1980. https://doi.org/10.1016/0141-0296(80)90002-4.
[14] Morris E, Szabo V, Yang G, Isaacson M. Frequency domain dynamic analysis of a floating bridge. In: Coastal structures 2003 - proceedings of the conference; 2003. https://doi.org/10.1061/40733(147)110.
[15] Xu Y, Øiseth O, Moan T, Naess A. Prediction of long-term extreme load effects due to wave and wind actions for cable-supported bridges with floating pylons. Eng Struct 2018. https://doi.org/10.1016/j.engstruct.2018.06.023.
[16] Cheng Z, Gao Z, Moan T. Extreme responses and associated uncertainties for a long end-anchored floating bridge. Eng Struct 2020. https://doi.org/10.1016/j.engstruct.2020.110858.
[17] Sha Y, Amdahl J, Aalberg A, Yu Z. Numerical investigations of the dynamic response of a floating bridge under environmental loadings. Ships Offshore Struct 2018;13:113–26. https://doi.org/10.1080/17445302.2018.1426818.
[18] Viuff T, Leira BJ, Xiang X, Øiseth O. Effects of wave directionality on extreme response for a long end-anchored floating bridge. Appl Ocean Res 2019;90. https://doi.org/10.1016/j.apor.2019.05.028.
[19] Cheng Z, Gao Z, Moan T. Wave load effect analysis of a floating bridge in a fjord considering inhomogeneous wave conditions. Eng Struct 2018. https://doi.org/10.1016/j.engstruct.2018.02.066.
[20] Fredriksen AG, Heiervang MF, Larsen PN, Sandnes PG, Sørby B, Bonnemaire B, Nesteby A, Nedrebø Ø. Hydrodynamical aspects of pontoon optimization for a side-anchored floating bridge. J Offshore Mech Arctic Eng 2019. https://doi.org/10.1115/1.4042420.
[21] Viuff T, Xiang X, Leira BJ, Øiseth O. Software-to-Software comparison of end-anchored floating bridge global analysis. J Bridge Eng 2020. https://doi.org/10.1061/(asce)be.1943-5592.0001545.
[22] Giske FIG, Kvåle KA, Leira BJ, Øiseth O. Long-term extreme response analysis of a long-span pontoon bridge. Mar Struct 2018;58:154–71. https://doi.org/10.1016/j.marstruc.2017.11.010.
[23] Chakrabarti S. Hydrodynamic interaction forces on multi-moduled structures. Ocean Eng 2000;27:1037–63. https://doi.org/10.1016/S0029-8018(99)00034-7.
[24] Kagemoto H, Yue DKP. Hydrodynamic interaction analyses of very large floating structures. Mar Struct 1993;6:295–322. https://doi.org/10.1016/0951-8339(93)90025-X.
[25] Kashiwagi M. Hydrodynamic interactions among a great number of columns supporting a very large flexible structure. J Fluid Struct 2000. https://doi.org/10.1006/jfls.2000.0306.
[26] Maniar HD, Newman JN. Wave diffraction by a long array of cylinders. J Fluid Mech 1997;339:309–30. https://doi.org/10.1017/S0022112097005296.
[27] Newman JN. Wave effects on multiple bodies. Hydrodyn. Sh. Ocean Eng. 2001;2001:3–26.
[28] Siddorn P, Eatock Taylor R. Diffraction and independent radiation by an array of floating cylinders. Ocean Eng 2008;35:1289–303. https://doi.org/10.1016/j.oceaneng.2008.06.003.
[29] Feng X, Bai W. Wave resonances in a narrow gap between two barges using fully nonlinear numerical simulation. Appl Ocean Res 2015;50:119–29. https://doi.org/10.1016/j.apor.2015.01.003.
[30] Lu L, Teng B, Sun L, Chen B. Modelling of multi-bodies in close proximity under water waves - fluid forces on floating bodies. Ocean Eng 2011;38:1403–16. https://doi.org/10.1016/j.oceaneng.2011.06.008.
[31] Perić M, Swan C. An experimental study of the wave excitation in the gap between two closely spaced bodies, with implications for LNG offloading. Appl Ocean Res 2015;51:320–30. https://doi.org/10.1016/j.apor.2015.01.010.
[32] Chen X. Hydrodynamics in offshore and naval applications - part I. 6th Int. Conf. Hydrodyn 2004.
[33] Faltinsen OM, Rognebakke OF, Timokha AN. Two-dimensional resonant piston-like sloshing in a moonpool. J Fluid Mech 2007. https://doi.org/10.1017/S002211200600440X.
[34] Huijsmans RHM, Pinkster JA. Diffraction and radiation of waves around side-by-side moored vessels. R.H.M. I; 2001.
[35] Williams AN, Demirbilek Z. Hydrodynamic interactions in floating cylinder arrays-I. Wave scattering. Ocean Eng 1988. https://doi.org/10.1016/0029-8018(88)90002-9.
[36] Feng X, Bai W, Chen XB, Qian L, Ma ZH. Numerical investigation of viscous effects on the gap resonance between side-by-side barges. Ocean Eng 2017;145:44–58. https://doi.org/10.1016/j.oceaneng.2017.08.060.
[37] Kara F. Multibody interactions of floating bodies with time-domain predictions. J Waterw Port, Coast Ocean Eng 2020;146:04020031. https://doi.org/10.1061/(asce)ww.1943-5460.0000588.
[38] Li B. Multi-body hydrodynamic resonance and shielding effect of vessels parallel and nonparallel side-by-side. 2020. https://doi.org/10.1016/j.oceaneng.2020.108188.

[39] Molin B, Remy F, Kimmoun O, Stassen Y. Experimental study of the wave propagation and decay in a channel through a rigid ice-sheet. Appl Ocean Res 2002;24:247–60. https://doi.org/10.1016/S0141-1187(03)00005-1.
[40] Nam BW, Kim Y, Hong SY. Hydrodynamic interaction between two barges during berthing operation in regular waves. Ocean Eng 2015;106:317–28. https://doi.org/10.1016/j.oceaneng.2015.07.011.
[41] Wang H, Zhao W, Draper S, Wolgamot HA, Taylor PH. Experimental and numerical study of free-surface wave resonance in the gap between two elongated parallel boxes with square corners. Appl Ocean Res 2020;104. https://doi.org/10.1016/j.apor.2020.102376.
[42] Xiang X, Miao Q, Chen X, Kuang X. Validation on coupled motion responses of two interacting ships in waves. 5th Int. Work. Sh. Hydrodyn. 2007:103–8.
[43] Xiang X, Faltinsen OM. Maneuvering of two interacting ships in calm water. 11th Int. Symp. Pract. Des. Ships Other Float. Struct PRADS 2010;1:161–71. https://doi.org/10.1007/bf03449294. 2010.
[44] Zhao W, Pan Z, Lin F, Li B, Taylor PH, Efthymiou M. Estimation of gap resonance relevant to side-by-side offloading. Ocean Eng 2018;153:1–9. https://doi.org/10.1016/j.oceaneng.2018.01.056.
[45] Eatock Taylor R, Sun L, Taylor PH. Gap resonances in focused wave groups. In: Proceedings of 23rd international workshop on water waves and floating bodies; 2008.
[46] Tajali Z, Shafieefar M. Hydrodynamic analysis of multi-body floating piers under wave action. Ocean Eng 2011;38:1925–33. https://doi.org/10.1016/j.oceaneng.2011.09.025.
[47] Viuff T, Xiang X, Øiseth O, Leira BJ. Model uncertainty assessment for wave- and current-induced global response of a curved floating pontoon bridge. Appl Ocean Res 2020. https://doi.org/10.1016/j.apor.2020.102368.
[48] Xiang X, Løken A. Hydroelastic analysis and validation of an end-Anchored floating bridge under wave and current loads. In: Proceedings of the international conference on offshore mechanics and arctic engineering - omae; 2019. https://doi.org/10.1115/OMAE2019-95114.
[49] Xiang X, Viuff T, Leira B, Øiseth O. Impact of hydrodynamic interaction between pontoons on global responses of a long floating bridge under wind waves. In: Proceedings of the ASME 2018 37th international conference on ocean, offshore and arctic engineering OMAE2018; 2018. https://doi.org/10.1115/OMAE2018-78625.
[50] Dassault Systèmes Simulia, Fallis A, Techniques D. ABAQUS documentation. Abaqus 2013;6:12. https://doi.org/10.1017/CBO9781107415324.004.
[51] Scanlan RH. The action of flexible bridges under wind, II: buffeting theory. J Sound Vib 1978;60:201–11. https://doi.org/10.1016/S0022-460X(78)80028-5.
[52] DNV GL. Wadam: wave analysis by diffraction and Morison theory. 2017.
[53] Orcina Ltd. OrcaWave. 2020.
[54] Statens vegvesen. MetOcean design basis. 2018.
[55] Skamarock WC, Klemp JB, Dudhia J, Gill DO, Liu Z, Berner J, Wang W, Powers JG, Duda MG, Barker DM, Huang XY. A description of the advanced research WRF version 4. 2019.
[56] Booij N, Holthuijsen LH, Ris RC. The "swan" wave model for shallow water. Coast. Eng. 1996, Proceedings 2021:668–76. https://doi.org/10.1061/9780784402429.053.
[57] Statens vegvesen. AMC status 2 - concept evaluation. 2019.
[58] Statens vegvesen. N400 Handbook for bridge design. 2009.
[59] Kristensen V. (Statens vegvesen) Concept Development for floating bridge over Bjørnafjorden. Final report. Oslo, Norway. In: Report No: SBJ-33 -C5-OON-22 -RE-01 structural response analyses appendix C – coupled analyses; 2019.
[60] Storheim M. (Statens vegvesen) Concept Development for floating bridge over Bjørnafjorden. Final report. In: Report No:SBJ-33-C5-AMC-90-RE-107 appendix G –global analyses –response–K12; 2019. Oslo, Norway.